High Resolution 3D Winds Derived from a Modified WISSDOM Synthesis Scheme using Multiple Doppler Lidars and Observations

Chia-Lun Tsai[1], Kwonil Kim[1], Yu-Chieng Liou[2], and GyuWon Lee*[1]

[1]Department of Astronomy and Atmospheric Sciences, Center for Atmospheric REmote sensing (CARE), Kyungpook National University, Daegu, South Korea

[2]Department of Atmospheric Sciences, National Central University, Jhongli, Taiwan

* Corresponding author: Prof. GyuWon Lee, E-mail: gyuwon@knu.ac.kr

Abstract

A WISSDOM (Wind Synthesis System using Doppler Measurements) synthesis scheme was developed to derive high-resolution 3-dimensional (3D) winds under clear-air conditions. From this variational-based scheme, detailed wind information was obtained from scanning Doppler lidars, automatic weather stations (AWS), sounding observations, and local reanalysis datasets (LDAPS, Local Data Assimilation and Prediction System), which were utilized as constraints to minimize the cost function. The objective of this study is to evaluate the performance and accuracy of derived 3D winds from this modified scheme. A strong wind event was selected to demonstrate its performance over complex terrain in Pyeongchang, South Korea. The size of the test domain is 12×12 km^2 extended up to 3 km height mean sea level (MSL) with remarkably high horizontal and vertical resolution of 50 m. The derived winds reveal that reasonable patterns were explored from a control run, as they have high similarity with the sounding observations. The results of intercomparisons show that the correlation coefficients between derived horizontal winds and sounding observations are 0.97 and 0.87 for u- and v-component winds, respectively, and the averaged bias (root mean square deviation, RMSD) of horizontal winds is between -0.78 and 0.09 (1.72 and 1.65) m s^{-1}. The correlation coefficients between WISSDOM-derived winds and lidar QVP (quasi-vertical profile) are 0.84 and 0.35 for u- and v-component winds, respectively, and the averaged bias (RMSD) of horizontal winds is between 2.83 and 2.26 (3.69 and 2.92) m s^{-1}. The statistical errors also reveal a satisfying performance of the retrieved 3D winds; the median values of wind directions are $-5\sim5$ ($0\sim2.5$) degrees, the wind speed is approximately $-1\sim3$ m s^{-1} ($-1\sim0.5$ m s^{-1}) and the vertical velocity is $-0.2\sim0.6$ m s^{-1} compared with the lidar QVP (sounding observations). A series of sensitivity tests with different weighting coefficients, radius of influence (RI) in interpolation and various combination of different datasets were also performed, and the results indicate that the present setting of the control run is the optimal reference to WISSDOM synthesis in this event.

1. Introduction

In the past few decades, many practical methods have been developed to derive wind information by using meteorological radar data (Mohr and Miller, 1983, Lee et al., 1994, Liou and Chang, 2009, Bell et al. 2012). The derived winds substantially revealed reasonable patterns compared with conventional observations (such as surface stations, soundings, wind profiles, etc.) and models (Liou et al., 2014, North et al., 2017, Chen, 2019, Oue et al., 2019). Most comprehensive applications of the derived winds were adopted to document kinematic and precipitation structures associated with various weather systems at different scales like typhoon, tropical cyclone rainband, and non-precipitation low-pressure system (LPS) (Yu and Tsai, 2013, Yu and Tsai, 2017, Tsai et al. 2018, Yu et al., 2020, Cha and Bell, 2021, Tsai et al., 2022). In addition, the accuracy of 3D winds could be improved when increasing the numbers of Doppler radar because relatively fewer assumptions and more information can be included (Yu and Tsai 2010, Liou and Chang, 2009). Therefore, the retrieved schemes within multiple Doppler radars are a more popular way to obtain high-quality 3D winds and have been extensively applied to meteorological analyses.

The technique of velocity track display (VTD, Lee et al., 1994) and ground-based velocity track display (GBVTD, Lee et al., 1999) can derive the winds from single Doppler radar under some assumptions, as the wind patterns are generally uniform or axisymmetric rotational (Cha and Bell, 2021). More extended techniques based on VTD and GBVTD have also been applied to increase the quality of derived wind data, and such techniques include Extended-GBVTD (EGBVTD, Liou et al., 2006) and generalized velocity track display (GVTD, Jou et al., 2008). However, winds usually present nonuniform patterns and fast-evolving characteristics in most mesoscale weather systems and microscale phenomena, and complete and detailed winds are still difficult to resolve by these techniques. Based on the contexts of weaknesses from above schemes on the wind retrievals. Instead of a single Doppler radar, multiple Doppler can retrieve better quality 3D winds with relativity fewer assumptions because they provide sufficient radial velocity

67   measurements and wind information with wider coverage in the synthesis domain.

68   Cartesian Space Editing, Synthesis, and Display of Radar Fields under Interactive Control

69   (CEDRIC, Mohr and Miller, 1983) is a traditional package used to retrieve 3D winds by dual-

70   Doppler radar observations. This scheme usually determines the horizontal winds by using two

71   radars, and the vertical velocity can be obtained by variational adjustment with anelastic

72   continuity equation. Spline Analysis at Mesoscale Utilizing Radar and Aircraft Instrumentation

73   (SAMURAI) software is another way to retrieve 3D winds (Bell et al., 2012); this scheme is a

74   kind of variational data assimilation that adopts multiple radars. Recently, Tsai et al. (2018)

75   utilized the measurements of six Doppler radars to document precipitation and airflow structures

76   over complex terrain on the northeastern coast of South Korea via WISSDOM (Wind Synthesis

77   System using Doppler Measurements). The first purpose and details of algorithms can be found

78   in Liou and Chang (2009). Performing immersed boundary method (IBM, Tseng and Ferziger,

79   2003) in WISSDOM and its scientific applications were clearly documented in Liou et al. (2012),

80   and Liou et al. (2016), respectively. Since one of the advantages of WISSDOM is that it considers

81   the orographic forcing on Cartesian coordinates by applying the IBM, higher quality 3D winds

82   can be derived well over terrain (Liou et al., 2013, 2014, Lee et al., 2018).

83   Generally, radial velocity is measured by detecting the movement of precipitation particles

84   relative to the locations of Doppler radars; thus, there are no sufficient radial velocity

85   measurements under clear-air conditions. However, the winds in clear-air conditions usually play

86   an important role in the initiations of various weather systems and phenomena, such as downslope

87   winds, gap winds, and wildfires (Reed, 1931, Colle and Mass, 2000, Mass and Ovens, 2019, Lee

88   et al., 2020). Although surface stations, soundings, and wind profilers can measure winds under

89   clear-air conditions, relatively poor spatial coverage is still a problem for obtaining sufficient

90   wind information in certain local areas. Therefore, scanning Doppler lidars will be one approach

91   to obtain wind information under clear-air conditions. Päschke et al. (2015) assessed the quality

92   of wind derived by Doppler lidar with a wind profiler in a year trial, and the results showed good

93   agreement in wind speed (the error ranged between 0.5 and 0.7 m s^{-1}) and wind direction (the

94   error ranged between 5° and 10°). Bell et al. (2020) combined an intersecting range height

95   indicator (RHI) of six Doppler lidars to build "virtual towers" (such as wind profilers) to

96   investigate the airflow over complex terrain during the Perdigão experiment. These virtual towers

97   can fill the gap in wind measurements above meteorological towers. The uncertainty of wind

98   fields is also reduced by adopting multiple Doppler lidars (Choukulkar et al., 2017), and a high

99   spatiotemporal resolution of derived wind is allowed to check small-scale rotors in mountainous

100   areas (Hill et al., 2010).

101   The original WISSDOM was designed to retrieve 3D winds based on Doppler radar

102   observations and background inputs combined with conventional observations and modeling.

103   However, the original WISSDOM only provided 3D winds under precipitation conditions, and it

104   cannot work well under clear-air conditions because the Doppler radar is not easy to detect radial

105   velocity without precipitation particles. To obtain high-quality 3D winds under clear-air

106   conditions for investigating the initiations of precipitation systems in advance of rain and snow

107   formatted. The radial velocity observed from the scanning Doppler lidars can be used in

108   WISSDOM, which is the most important benefit rather than Doppler radar in related research

109   topics. Furthermore, the conventional observations and modeling datasets were used as isolated

110   constraints in the modified WISSDOM synthesis scheme. One of the benefits of the isolated

111   constraints is that it is easy to synthesize any kind of wind information obtained from available

112   datasets and give suitable weighting coefficients with different constraints when they are

113   processing the minimization in the cost function. Thus, more reliable 3D winds in clear-air

114   conditions were well derived from this modified WISSDOM synthesis scheme.

115   The objective of this study is to modify the WISSDOM synthesis scheme based on the

116   original version to be a more flexible and useful scheme by adding any number of Doppler lidars

117   and conventional observations as well as modeling datasets. This modified WISSDOM will allow

118   us to obtain an exceedingly high spatial resolution of 3D winds (50 m was set in this study) under

clear-air conditions. It is because the Doppler lidar had high spatial resolution in between 40 and

60 m horizontally, however, the Doppler radar had relatively low spatial resolution from

approximately 100 to 1000 m. A variety of adequate datasets were collected during a strong wind

event in the winter season during an intensive field experiment ICE-POP 2018 (International

Collaborative Experiments for Pyeongchang 2018 Olympic and Paralympic winter games). In

summary, the main goal of this study is to use Doppler lidar observations to retrieve high-

resolution 3D winds over terrain under clear-air conditions via WISSDOM. In this study, detailed

principles of the modified WISSDOM and data implementation are elucidated in the following

sections. In addition, the modified WISSDOM was performed to retrieve 3D winds over complex

terrain under clear-air conditions in a strong wind event. The reliability of the derived 3D winds

was also evaluated with conventional observations.

2. Methodology

2.1 Original version of WISSDOM (WInd Synthesis System using DOppler Measurements)

WISSDOM is a mathematically variational-based scheme to minimize the cost function, and

various wind-related observations can be used as one of the constraints in the cost function. The

3D winds were derived by variationally adjusted solutions to satisfy the constraints in the cost

function, thus the results of retrieved winds were the analytic expression in this scheme. The

original version of WISSDOM performed five constraints, including radar observations (i.e.,

reflectivity and radial velocity), background (combined with automatic weather stations,

sounding, model or reanalysis data), continuity equation, vorticity equation, and Laplacian

smoothing (Liou and Chang 2009). Liou et al. (2012) applied the IBM in WISSDOM to consider

the affecting upon nonflat surface, one of advantages in IBM is providing realistic topographic

forcing without the need to change the Cartesian coordinate system into a terrain-following

142   coordinate system. More scientific documentations associated with the interactions between

143   terrain, precipitation and winds in different areas can be referred to Liou et al. (2016, Taiwan),

144   and Tsai et al. (2018, South Korea). The cost function can be expressed as

145
$$J = \sum_{M=1}^{5} J_M,$$
(1)

146   where J_M is the different constraints. J_1 is the constraint related to the geometric relation

147   between radar radial Doppler velocity observations (V_r) and derived one from true winds ($\mathbf{V}_t =$

148   $u_t\mathbf{i} + v_t\mathbf{j} + w_t\mathbf{k}$) in Cartesian coordinates [eq. (2)]. Note that the $\mathbf{V}_t$ will be first guessed

149   random resulting from sounding, modeling, or equal zero if there is not any information about

150   wind in beginning.

151
$$J_1 = \sum_{t=1}^{2} \sum_{x,y,z} \sum_{i=1}^{N} \alpha_{1,i} \left(T_{1,i,t}\right)^2.$$
(2)

152   Since WISSDOM is a scheme that uses the 4DVAR approach, the variations between different

153   time steps (t) should be considered, and two time steps of radar observations were collected in

154   this constraint and all following constraints. The x, y, z indicates the locations of a given grid

155   point in the synthesis domain, and i could be any number (N) of radars (at least 1). The α_1 is

156   the weighting coefficient of J_1 (α_2 is the weighting coefficient of J_2 and so on). $T_{1,i,t}$ in eq.

157   (2) is defined as eq. (3):

158
$$T_{1,i,t} = (V_r)_{i,t} - \frac{\left(x - P_x^i\right)}{r_i} u_t - \frac{\left(y - P_y^i\right)}{r_i} v_t - \frac{\left(z - P_z^i\right)}{r_i}\left(w_t - W_{T,t}\right),$$
(3)

159   $(V_r)_{i,t}$ is the radial velocity observed by the radar (i) at time step (t), P_x^i, P_y^i and P_z^i depict the

160   coordinate of radar i. The u_t, v_t and w_t ($W_{T,t}$) denote the 3D winds (terminal velocity of

161   precipitation particles) at given grid points at the time step t ; and $r_i =$

162   $\sqrt{(x - P_x^i)^2 + (y - P_y^i)^2 + (z - P_z^i)^2}.$

163   The second constraint is the difference between the background ($\mathbf{V}_{B,t}$) and true (derived)

164   wind field ($\mathbf{V}_t = u_t\mathbf{i} + v_t\mathbf{j} + w_t\mathbf{k}$), which is defined as

165
$$J_2 = \sum_{t=1}^{2} \sum_{x,y,z} \alpha_2 \left(\mathbf{V}_t - \mathbf{V}_{B,t} \right)^2. \tag{4}$$

166 There were several options to obtain background in the original version of WISSDOM. The most

167 popular background resource involves using sounding observations; however, it can only provide

168 homogeneous wind information for each level in WISSDOM with relatively coarse temporal

169 resolution (3- to 12-hour intervals). The other option is combining sounding observations with

170 AWS (automatic weather station) observations. Although the AWS provided wind information

171 with better temporal resolution (1-min), the data were only observed at the surface layer with

172 semirandom distributions. The last option is to combine sounding, AWS, modeling or reanalysis

173 datasets. However, various datasets with different spatiotemporal resolutions are not favorable

174 for appropriate interpolation of given grid points of WISSDOM synthesis, and the accuracy and

175 reliability of the background may have been significantly affected by such a variety of datasets.

176 Thus, these different observed or model data should be treated differently to minimize the

177 uncertainties and improve the accuracy. Thus, one of the improvements in the modified

178 WISSDOM is that these inputs were separated into independent constraints individually. Note

179 that the sounding observations are still a necessary dataset because the air density and temperature

180 profile were used to identify the height of the melting level. In this study, sounding winds were

181 adopted to represent the background for each level and a constraint at the same time; nevertheless,

182 the AWS and reanalysis dataset are independent constraints in the modified WISSDOM (details

183 are provided in the following section).

184 The third, fourth and fifth constraints in the cost function are the anelastic continuity

185 equation, vertical vorticity equation and Laplacian smoothing filter, respectively. Equations (5),

186 (6) and (7) are denoted as follows:

187
$$J_3 = \sum_{t=1}^{2} \sum_{x,y,z} \alpha_3 \left[\frac{\partial(\rho_0 u_t)}{\partial x} + \frac{\partial(\rho_0 v_t)}{\partial y} + \frac{\partial(\rho_0 w_t)}{\partial z} \right]^2, \tag{5}$$

188 $$J_4 = \sum_{x,y,z} \alpha_4 \left\{ \frac{\partial \zeta}{\partial t} + \overline{\left[u\frac{\partial \zeta}{\partial x} + v\frac{\partial \zeta}{\partial y} + w\frac{\partial \zeta}{\partial z} + (\zeta + f)\left(\frac{\partial u}{\partial x} + \frac{\partial v}{\partial y}\right) + \left(\frac{\partial w}{\partial x}\frac{\partial v}{\partial y} - \frac{\partial w}{\partial y}\frac{\partial u}{\partial z}\right)\right]} \right\}^2 , \quad (6)$$

189 $$J_5 = \sum_{t=1}^{2} \sum_{x,y,z} \alpha_5 [\nabla^2 (u_t + v_t + w_t)]^2 . \quad (7)$$

190 ρ_0 in eq. (5) is the air density, and $\zeta = \partial v/\partial x - \partial u/\partial y$ in eq. (6). The main advantage is that

191 the use of vertical vorticity can provide further improvement in winds and thermodynamic

192 retrievals.

193 **2.2 The modified WISSDOM**

194   In addition to the five constraints in the original version, the modified WISSDOM synthesis

195 scheme includes three more constraints in the cost function. Thus, the cost function in the

196 modified WISSDOM was written as

197 $$J = \sum_{M=1}^{8} J_M . \quad (8)$$

198     $J_1 \sim J_5$ in (8) are the same constraints corresponding to equations (2)-(7). The main purpose

199 of this study is to retrieve 3D winds under clear-air conditions in which observational data are

200 relatively rare. Instead of the radial velocity $(V_r)_{i,t}$ observed from Doppler radars in eq. (3) in

201 original version of WISSDOM, the radial velocity observed from Doppler lidars was adopted in

202 the modified WISSDOM synthesis. In addition, if there were no precipitation particles under

203 clear-air conditions, the terminal velocity of precipitation particles $(W_{T,t})$ was set to zero in eq.

204 (3) in the modified WISSDOM. The time steps in WISSDOM of this study were set by the

205 synthesis time and 12 mins before the synthesis time due to the temporal resolution of main input

206 lidar data is 12 mins.

207   The sixth constraint is the difference between the derived wind fields and the sounding

208 observations $(\mathbf{V}_{S,t})$, as defined in (9):

$$J_6 = \sum_{t=1}^{2} \sum_{x,y,z} \alpha_6 (V_t - V_{S,t})^2. \tag{9}$$

210   The sounding data in J_6 were interpolated to the given grid points near its tracks bearing on the

211   radius influence (RI) distance (the details are provided in Section 3.2.3). The main difference

212   between J_6 and J_2 is that the sounding data were used as an observation for given 3D locations,

213   instead of the constraint of homogeneous background winds for each level in the studied domain.

214   The seventh constraint represents the discrepancy between the true (derived) wind fields and

215   AWS ($V_{A,t}$), as expressed in (8):

$$J_7 = \sum_{t=1}^{2} \sum_{x,y,z} \alpha_7 (V_t - V_{A,t})^2. \tag{8}$$

217   Finally, the eighth constraint measures the misfit between the derived winds and the local

218   reanalysis dataset ($V_{L,t}$), as defined in (9):

$$J_8 = \sum_{t=1}^{2} \sum_{x,y,z} \alpha_8 (V_t - V_{L,t})^2. \tag{9}$$

220   In this study, various observations and reanalysis datasets were utilized as constraints in the cost

221   function of WISSDOM. The most important dataset is the radial velocity observed from Doppler

222   lidars, which can measure wind information with high spatial resolution and good coverage from

223   near the surface up to higher layers in the test domain. Sounding and AWS can provide horizontal

224   winds for background or to be included in the constraints. The local reanalysis datasets were

225   obtained from the 3DVAR Local Data Assimilation and Prediction System (LDAPS) data

226   assimilation system from the Korea Meteorological Administration (KMA). Since these datasets

227   have different coordinate systems and various spatiotemporal resolutions, additional procedures

228   are required before the synthesis. Detailed descriptions of the procedures are described in the next

229   section.

230   The high-quality synthesized 3D wind field from radar observations has been applied in

231   several previous studies such as those by Liou and Chang (2009), Liou et al. (2012, 2013, 2014,

232 2016), and Lee et al. (2017). The advantages and details of the WISSDOM can be found in Tsai

233 et al. (2018). Although there were quite a few studies by using Doppler radar in WISSDOM, this

234 study is first time to apply the Doppler lidar data in WISSDOM. This modified WISSDOM

235 synthesis scheme has also been applied in the analysis related to the mechanisms of

236 orographically induced strong wind on the northeastern coast of Korea (Tsai et al., 2022). In

237 different view standing from previous studies, this study provides clear context, detail procedures,

238 reliability, and the limitations of the modified WISSDOM.

3. Data processing with a strong wind event

3.1 Basic information of WISSDOM synthesis

241 A small domain near the northeastern coast of South Korea was selected to derive detailed

242 3D winds over complex terrain (in the black box in the inset map in Fig. 1) because relatively

243 dense and high-quality wind observations were only collected in this region during ICE-POP

244 2018. The size of the WISSDOM synthesis domain is 12×12 km^2 (up to 3 km MSL height) in

245 the horizontal (vertical) direction with 50 m grid spacing. Such high spatial resolution 3D winds

246 were synthesized every 1 hour in this test. Note that the output time steps are adjustable to be

247 finer (recommended limitation is 10 mins), but they are highly related to the temporal resolution

248 of various datasets and computing resources. Two scanning Doppler lidars are located near the

249 center of the domain: one is the equipped "WINDEX-2000" (the model's name from the

250 manufacturer) at the May Hills Supersite (MHS) site, and the other is the "Stream line-XR" at

251 the DaeGwallyeong regional Weather office (DGW) site. In addition to the operational AWS

252 (727 stations), additional surface observations (32 stations) are also involved in ICE-POP 2018

253 surrounding the MHS and DGW sites and the venues of the winter Olympic Games. The

254 soundings are launched at the DGW site every 3 hours during the research period. The LDAPS

255 also provided high spatial resolution of wind information in the test domain. The horizontal

256 distribution of all instruments and datasets used are shown in Fig. 1.
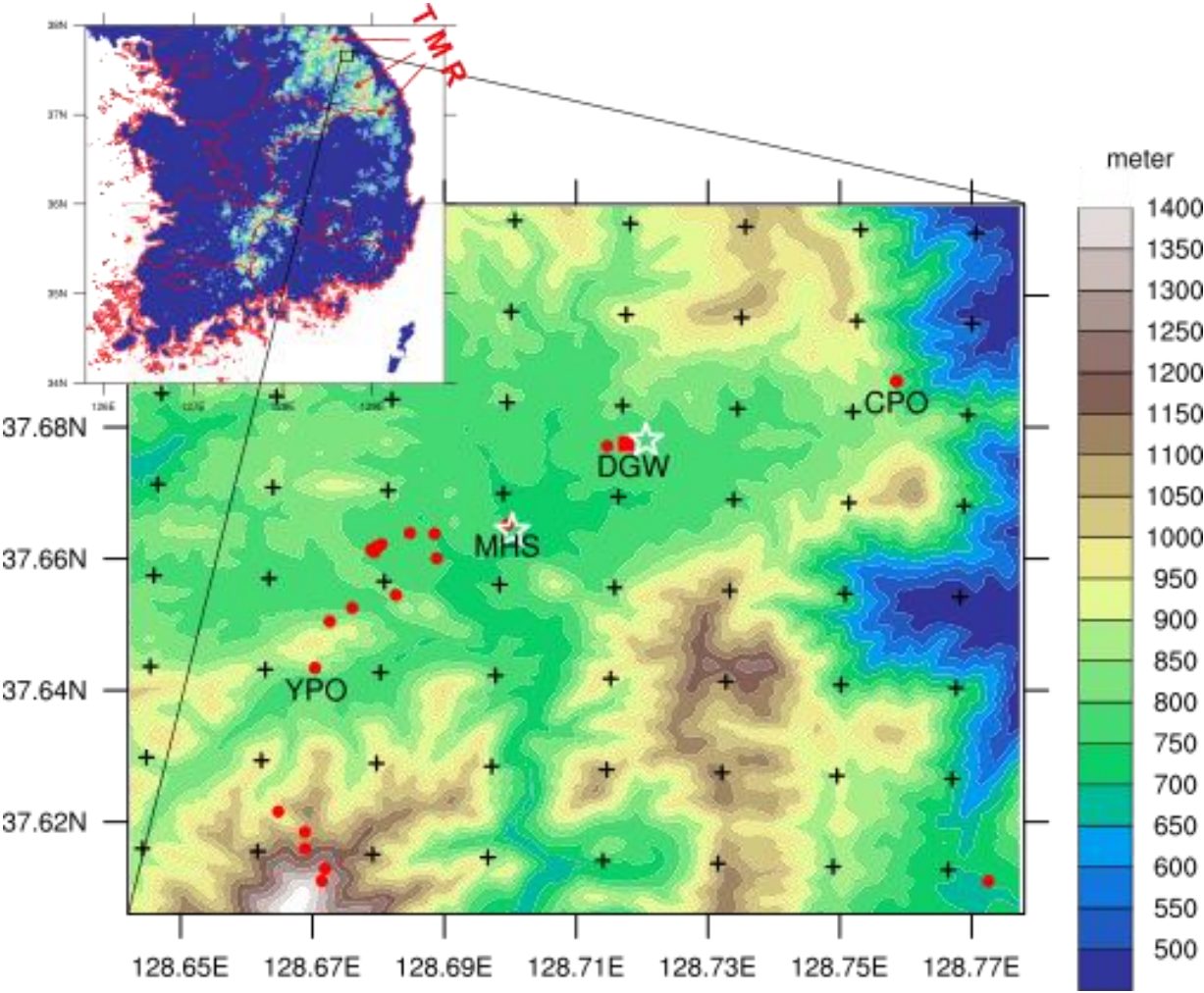
257
258 Figure 1. Horizontal distribution of instruments and datasets used in this study. A small box in the upper map

259   indicates the WISSDOM synthesis domain. The Doppler lidars are marked by start symbols at the MHS and

260   DGW sites. Red solid circles and square indicate the automatic weather station (AWS) and sounding, respectively.

261   The black cross marks the data points of LDAPS. Topographic features and elevations are shown with the color

262   shading in a color bar in the figure. The location of the Teabeak Mountain Range (TMR) is also marked.

263 **3.2 Data implemented in WISSDOM synthesis**

264 **3.2.1 Scanning Doppler lidars**

265   The radial velocity observed from two scanning Doppler lidars was utilized to retrieve 3D

266 winds via WISSDOM synthesis. The original coordinate system of observed lidar data is not a

267 Cartesian coordinate system, but spherical (or polar) coordinate system as plan position indicator

268   (PPI) and hemispheric range height indicator (HRHI) or RHI. Although relatively dense and

269   complete coverage of wind information (i.e., radial velocity of aerosols) were sufficiently

270   recorded by lidar observations, the collected data are usually not located directly on the given

271   grid points in the WISSDOM synthesis (i.e., Cartesian coordinate system). In this study, the lidar

272   data were interpreted simply from the lidar coordinate system to the Cartesian coordinate system

273   via bilinear interpolation.

274   The scanning strategy of the lidar at the DGW site includes five elevation angles for PPI (7°,

275   15°, 30°, 45°, and 80° before 10:00 UTC on 14 Feb. 2018 and 4°, 8°, 14°, 25°, and 80° after 10:00

276   UTC) and two HRHIs at azimuth angles of 51° and 330°. A full volume scan included all PPIs

277   and HRHIs every ~12 min. The maximum observed radius distance is ~13 km, and the grid

278   spacing is 40 m for each gate along the lidar beam. The scanning strategy of the lidar at the MHS

279   site involves seven elevation angles for PPI (5°, 7°, 10°, 15°, 30°, 45°, and 80°) and one HRHI

280   at an azimuth angle of 0°. A full volume scan included all PPIs and RHIs every ~12 min. The

281   maximum observed radius distance was ~8 km, and the grid spacing was 60 m. The vertical

282   distribution of lidar data in the test domain is shown as blue lines in Fig. 2a.

283   **3.2.2 Automatic weather station (AWS)**

284   Most of the AWS stations are not exactly located on the given grid points of the Cartesian

285   coordinate system. Objective analysis (Cressman, 1959) is a popular way to correct semirandom

286   and inhomogeneous meteorological fields into regular grid points. Note that the wind directions

287   and wind speed must first project with the values along u- and v-components then interpolate

288   their values individually to the given grids. This study adopted objective analysis for the AWS

289   observations with adjustable RI distances between 100 m and 2000 m. After this first step, the

290   observational data can reasonably interpolate to the given grid points horizontally. Furthermore,

291   an additional step is required to put these interpolated data into the given grid points at different

292   vertical levels because the AWS are located at different elevations in the test domain. In the

293   traditional way of original WISSDOM, the interpolated data are moved to the closest level with

294   the shortest distance just above the AWS site. However, the interpolated data are NOT moved to

295   the closest level if the shortest distances are large like more than half (50%) of grid spacing.

296   Nevertheless, to include more data from the AWS observations appropriately, adjusted distances

297   between the AWS sites and given grid points at different vertical levels were necessarily

298   considered. These adjusted distances can be named as vertical extension (VE) here, and there are

299   two options of 50% and 90% in the tests of this study, which correspond to 25 m and 45 m

300   extensions between each grid (in case of the grid spacing is 50 m), respectively. An example

301   demonstrated how to implement the interpolated data to the given grid points by adjustable VE

302   after step one (Fig. 2b).

303   In Fig. 2b, the interpolated data do not need to move to a given grid point (as an example, at

304   the 800 m level here) if the elevation of the AWS is equal to the height of a given grid point as

305   point A. When the AWS is located higher than a given grid point (as point B in Fig. 2b) and does

306   not reach the lower boundary of VE (50%) from the upper given grid point (i.e., at the 850 m

307   level), this interpolated data will be removed and wasted. In contrast, when the interpolated data

308   are located just below the given grid point with 50% VE, it will be achieved in the WISSDOM

309   synthesis at the 800 m level (point C in Fig. 2b). The interpolated data of point D have a similar

310   situation to point B; however, it will be achieved at the 800 m level because a higher VE (90%)

311   was applied here. Since the locations of the AWS are semirandom with relatively sparse or

312   concentrated distributions, the optimal RI and adjustable VE make it possible to include more

313   AWS observations in the WISSDOM synthesis.
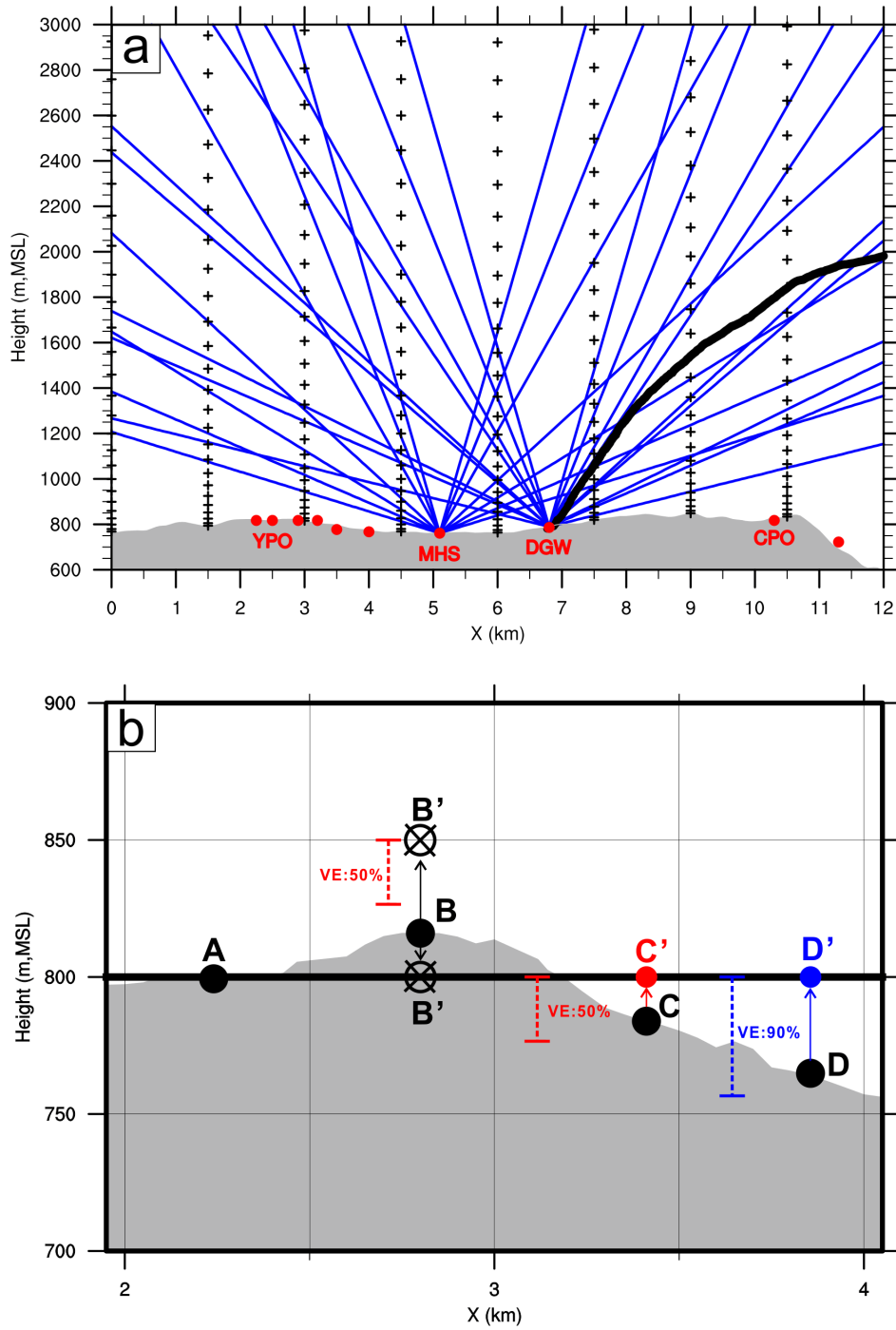
Figure 2. (a) Schematic diagram of the vertical distribution of adopted lidar datasets. Blue lines indicate the lidar data observed at the DGW and MHS sites with different elevation angles. The AWS stations are located on the ground and are marked by solid red circles. An example of a sounding track launched from the DGW site in one time step (06:00 UTC on 14 Feb. 2018) is plotted as a thick black line. The black cross marks indicate the vertical distribution of the LDAPS dataset. (b) Schematic diagram for data implementation with various locations of the AWS stations and different percentages of VE (vertical extension) from given grid points at the 800 m MSL level (thick black line). The gray shading on the bottom represents the topography.

3.2.3 Sounding

323   During ICE-POP 2018, the soundings are launched at the DGW site every 3 hours (from

324   00Z). Vertical profiles of air pressure, temperature, humidity, wind speed and directions were

325   recorded every second (i.e., ~3 m vertical spatial resolution) associated with the rising sensor.

326   The sounding sensor drifted when rising, and an example of its track in one time step is shown

327   as a thick black line in Fig. 2a. In this example, the sounding movement was mostly affected by

328   westerly winds, and it measured the meteorological parameters in any location along the track in

329   the test domain. The coordinate system of sounding data is quite similar to the distribution of

330   AWS measurements, and the observations are not located right on the given grid points of the

331   WISSDOM synthesis.

332   Similar to the AWS data, the sounding data also underwent objective analysis with an

333   adjustable RI distance for the wind measurements in the first step. Then, the interpolated data

334   were switched to given grid points for each vertical level by the different VE in the WISSDOM

335   synthesis.

336   **3.2.4 Reanalysis dataset: LDAPS**

337   The local reanalysis dataset LDAPS was generated by the KMA. This dataset provides u-

338   and v-component winds every 3 hours, and the horizontal spatial resolution is ~1.5 km with the

339   grid type in Lambert Conformal (as black cross marks in Fig. 1). The data revealed denser

340   distributions near the surface and sparse distributions at higher levels (see Fig. 2a). The initiations

341   of wind variables in the LDAPS were assimilated with many observational platforms, including

342   radar, AWS, satellite and sounding data. Thus, the relatively high reliability of this dataset could

343   be expected. In addition, such datasets have also significantly improved the forecast ability in

344   small-scale weather phenomena over complex terrain in Korea (Kim et al., 2019, Choi et al.,

345   2020, Kim et al., 2020).

346   The LDAPS data are not located directly on the given grid points of the WISSDOM synthesis

347   system. Unlike the distribution of AWS and sounding observations, LDAPS has dense and good

coverage in the test domain. The Cartesian coordinate is the most efficient way and the best system for partial differential equation (Armijo, 1969), then it also be used in the cost function of WISSDOM (Liou and Chang, 2009). Therefore, like lidar observations, the LDAPS data were also interpolated to the given grid points on the Cartesian coordinate system via the bilinear interpolation method.

3.3 Overview of the selected strong wind event

A strong wind event was selected to evaluate the performance of this modified WISSDOM synthesis scheme. In this strong wind event, the evolution of surface wind patterns on the Korean Peninsula was mainly dominated by a moving LPS which is one type of strong downslope winds (Park et al, 2022, Tsai et al., 2022). The LPS moved out from China and penetrated the northern part of the Korean Peninsula through the Yellow Sea beginning at approximately 12:00 UTC on 13 February 2018. Consequently, a relatively strong surface wind speed (exceeding ~17 m s^{-1}) was observed when the LPS was located near the northeastern coast of the Korean Peninsula (~130°E, 40°N) at 00:00 UTC on 14 February 2018 (Fig. 3). Then, the surface wind speed became weak when the LPS moved away from South Korea after 00:00 UTC on 15 February 2018 (not shown); the details of the synoptic conditions can be found in Tsai et al. (2022).

364
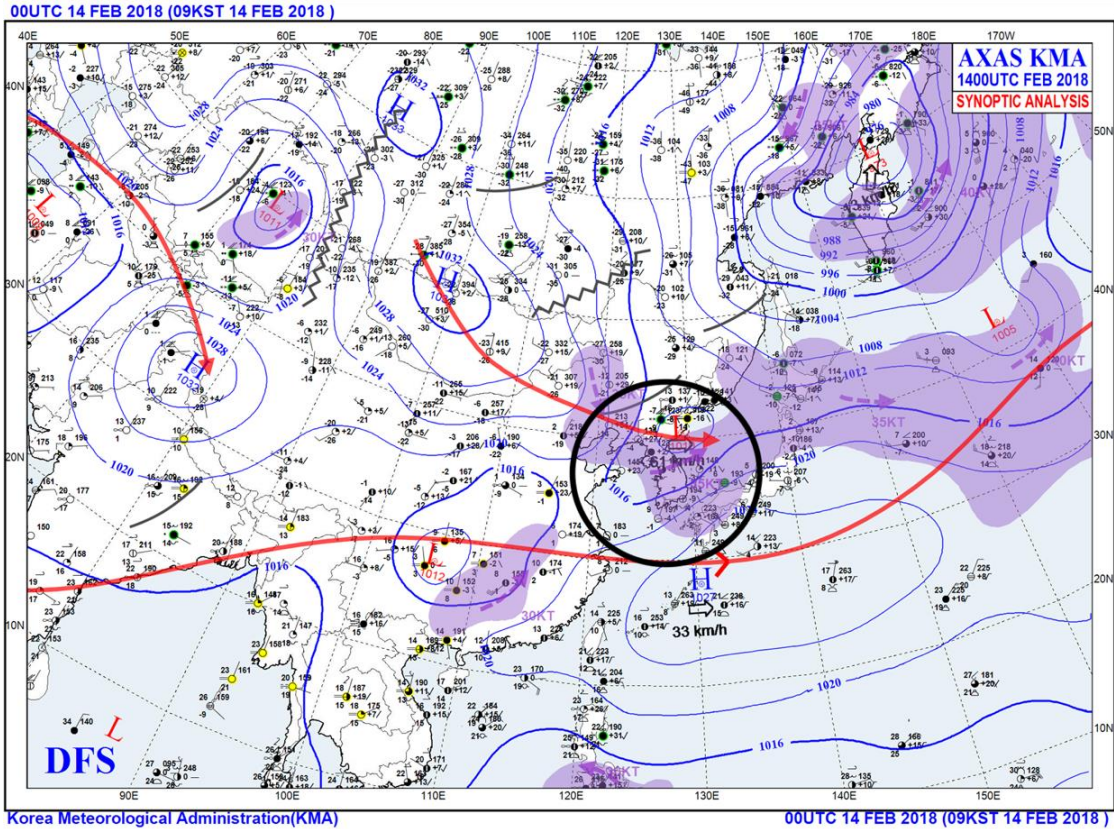
365 Figure 3. Synoptic surface chart from the Korea Meteorological Administration (KMA) at 00:00 UTC on 14 Feb.

366   2018. The locations of the Korean peninsula and the LPS has been marked by black circle.

367

368   This event is one of two strong wind events (i.e., daily maximum wind speeds larger than

369 10 m s^{-1} observed at the AWS sites along the northeastern coast of South Korea) in the past

370 decade based on the KMA historic record. Such a strong wind event may help us to examine the

371 potential maximum errors of the retrieved winds. Since persistent, strong westerly winds were

372 observed by the soundings and AWS from near the surface and upper layers over the TMR during

373 the event, the data coverages in the test domain were checked during a chosen time step (06:00

374 UTC on 14 February 2018). The percentage of data occupations for each dataset (after

375 interpolation) was checked, and the results are shown in Fig. 4. Note that the elevation of the

376 TMR is approximately 700 m MSL in the test domain. The lidars provided good coverage of

377 100% to 50% at the lower layers between 700 m and 800 m MSL. The coverage of lidars was

378 reduced significantly above 900 m MSL and remained at ~5% due to the scan strategy during the

379 Olympic games (more dense observations near the surface). The maximum coverage of the AWS

380   observations is ~40% at 800 m, and there was less coverage above this layer since relatively few

381   AWS stations are located in the higher mountains. Because only one sounding observation was

382   utilized in this domain, relatively few coverages were also depicted. The local reanalysis LDAPS

383   can provide complete coverage above 900 m MSL (exceeding 100%), albeit there was less

384   coverage in the lower layers due to terrain. The lidar, sounding, and AWS observations covered

385   most areas at lower levels but not higher levels; thus, the LDAPS compensated for most of the

386   wind information at the upper layers in the WISSDOM synthesis.
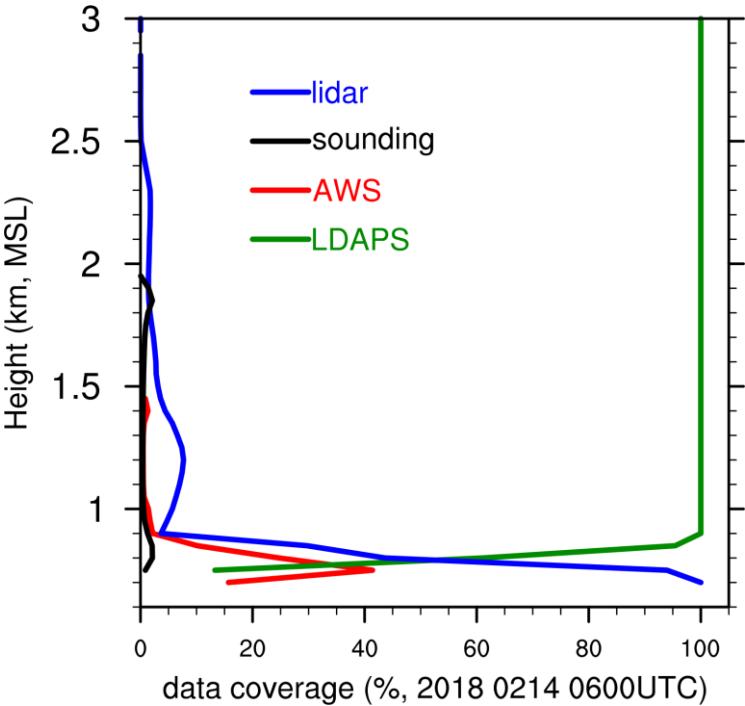
387

388   Figure 4. Data coverage (percentage, %) of the lidar (blue line), sounding (black line), AWS (red line) observations,

389   and LDAPS (green line) at 06:00 UTC on 14 Feb. 2018.

390   **4. Control run and the accuracy of WISSDOM**

391   **4.1 Control run**

392   Relatively reliable 3D winds were derived by a control run of the WISSDOM synthesis

393   because all available wind observations and local reanalysis datasets were appropriately acquired.

394   These datasets provided sufficient and complete wind information with a high percentage of

395 coverage in the test domain (cf. Fig. 4). Therefore, the retrieved winds from the control run can

396 be treated as the optimal results (i.e., analytic expression of variational-based scheme) in

397 WISSDOM. The control run was performed carefully with the necessary procedures in data

398 implementation before running the WISSDOM synthesis as follows. The lidar and LDAPS

399 datasets must perform bilinear interpolation to the given grid points in WISSDOM, and the

400 sounding and AWS observations must undergo objective analysis with the appropriate RI

401 distance and VE. The quantities of the weighting coefficients for each input dataset followed the

402 default setting from the original version of WISSDOM. The 3D winds were derived during one

403 time step at 06:00 UTC on 14 Feb. 2018 and compared with conventional observations. Note that

404 the best weights have been determined by a series of observation system simulation experiment

405 (OSSE) type tests from Liou and Chang (2009), they have putted more weights in observations

406 and less weights in modeling inputs. Based on the experiences and the default setting of weights

407 from previous studies, the basic setting of the control run has been first decided. The basic setting

408 of this control run is summarized in Table 1.

Table 1   Basic setting of WISSDOM (control run)

Domain Range	Latitude: 37.606°N~37.713°N Longitude: 128.642°E~128.778°E
Domain Size	12 × 12 × 3 km (long × width × vertical)
Spatial Resolution	0.05 × 0.05 × 0.05 km (long × width × vertical)
Terrain Resolution	0.09 km
Coordinate System	Cartesian coordinate system
Background	Sounding (DGW)
Data Implementation	Doppler Lidars (MHS, DGW): bilinear interpolation AWS: objective analysis (RI*: 1 km, VE*: 90%) Sounding (DGW): objective analysis (RI: 1 km, VE: 90%) LDAPS: bilinear interpolation
Weighting Coefficient (input datasets)	Doppler Lidars (α_1): 10^6 Background (α_2): 10^2 Sounding (α_6): 10^6 AWS (α_7): 10^6

LDAPS (α_8): 10^3

*RI: radius influence, VE: vertical extension

409   The results of 3D winds at 800 m MSL derived from the control run are shown in Figs. 5a,

410   c, and e. Topographic features comprised relatively lower elevations in the center of the test

411   domain, and there were weaker u-component winds (~7 m s^{-1}) near the AWS and MHS lidar sites

412   between 128.67°E and 128.71°E (Fig. 5a). In contrast, the u-component winds (~15 m s^{-1}) were

413   almost doubled near the DGW lidar site (between 128.71°E and 128.73°E). The vertical

414   structures of the u-component winds across these two lidars (i.e., along the black line in Fig. 5a)

415   are shown in Fig. 5b. The strength of the u-component winds rapidly increased from the surface

416   to the upper layers (from ~6 to 20 m s^{-1}), and uniform u-component winds with wavy pattern

417   were depicted above ~1 km MSL except for the stronger winds near the surface surrounding the

418   DGW site. There were relatively weak (strong) u-component winds surrounding the lidar at the

419   MHS (DGW) site near the surface. Relatively weak v-component winds were found

420   (approximately ±4 m s^{-1}) at 800 m MSL (Fig. 5c); thus, the horizontal wind directions were

421   mostly westerly winds during this time step. The v-component winds were obviously accelerated

422   in several local areas encompassing the terrain (near 128.71°E). The vertical structure of the v-

423   component winds (Fig. 5d) indicates that the v-component winds became stronger in the upper

424   layer. The wind directions were changed from westerly to southwesterly from the near surface

425   up to ~1.4 km MSL height. Updrafts were triggered on windward slopes when westerly winds

426   impinge the terrain or hills (Figs. 5e and 5f). Basically, the 3D winds derived from the WISSDOM

427   synthesis reveal reasonable patterns compared to synoptic environmental conditions (cf. Fig. 3);

428   the moving LPS accompanied stronger westerly winds.

429
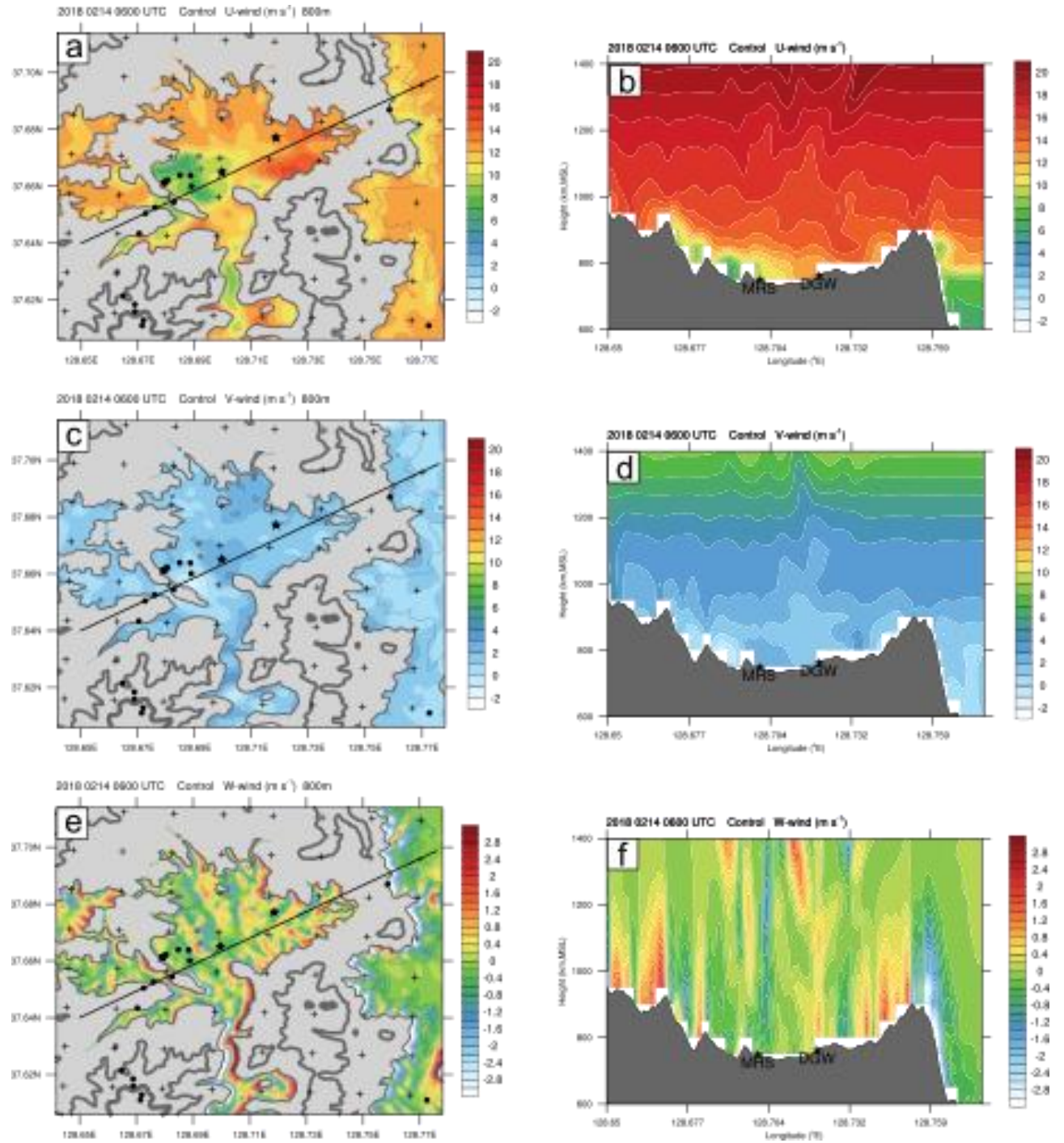
Figure 5. The 3D winds were derived from the control run by the WISSDOM synthesis at 06:00 UTC on 14 Feb. 2018. (a) The u-component winds (color, m s^{-1}) at 800 m MSL; the gray shading represents the terrain area, and the contours indicate different terrain heights of 600 m, 800 m and 1000 m MSL corresponding to thin to thick contours. The locations of lidars are marked with asterisks. (b) Vertical structures of u-component winds (color, m s^{-1}) along the black line in (a) The gray shading in the lower part of the figure indicates the height of the terrain. (c) and (d) are the same as (a) and (b) but for the v-component winds. (e) and (f) are the same as (a) and (b) but for the w-component winds.

4.2 Intercomparison between derived winds and observations

Detailed analyses were performed in this section to quantitatively evaluate the accuracy of the optimally derived 3D winds from the WISSDOM synthesis. Two kinds of instruments were available in the test domain to detect the relatively realistic winds: sounding and lidar quasi-vertical profiles (QVP, Ryzhkov et al., 2016), a profile of QVP can be general form a lidar. The horizontal winds observed from soundings and the 3D winds of the lidar QVP were utilized to represent observations. A complete analysis of the intercomparison between the WISSDOM synthesis and observations is presented in the following subsections.

4.2.1 Sounding

The discrepancies in horizontal winds derived from WISSDOM and the sounding observations for the entire research period (from 12:00 UTC on 13 to 12:00 UTC on 14 February 2018) were analyzed. Fig. 6 shows the scatter plots of the u- and v-component winds on the locations following the tracks of sounding launched from the DGW site. Most of the u-component winds derived from WISSDOM are in good agreement with the sounding observations, and the wind speed is increased with the height from approximately 10 to 40 m s^{-1}. Slight underestimation of retrieved u-component winds can be found at the layers of 1.5~2 km MSL (Fig. 6a). In contrast, most of the v-component winds were weak (smaller than 15 m s^{-1}) at all layers, because the environmental winds were more like westerlies during the research period. There were also slightly overestimated v-component winds derived from WISSDOM at the layers of 1.5~2 km MSL (Fig. 6b). The possible reason why the overestimated winds occurred above ~1.5 km MSL is that lidar data had relatively less coverages at higher layers (cf. Fig. 4).
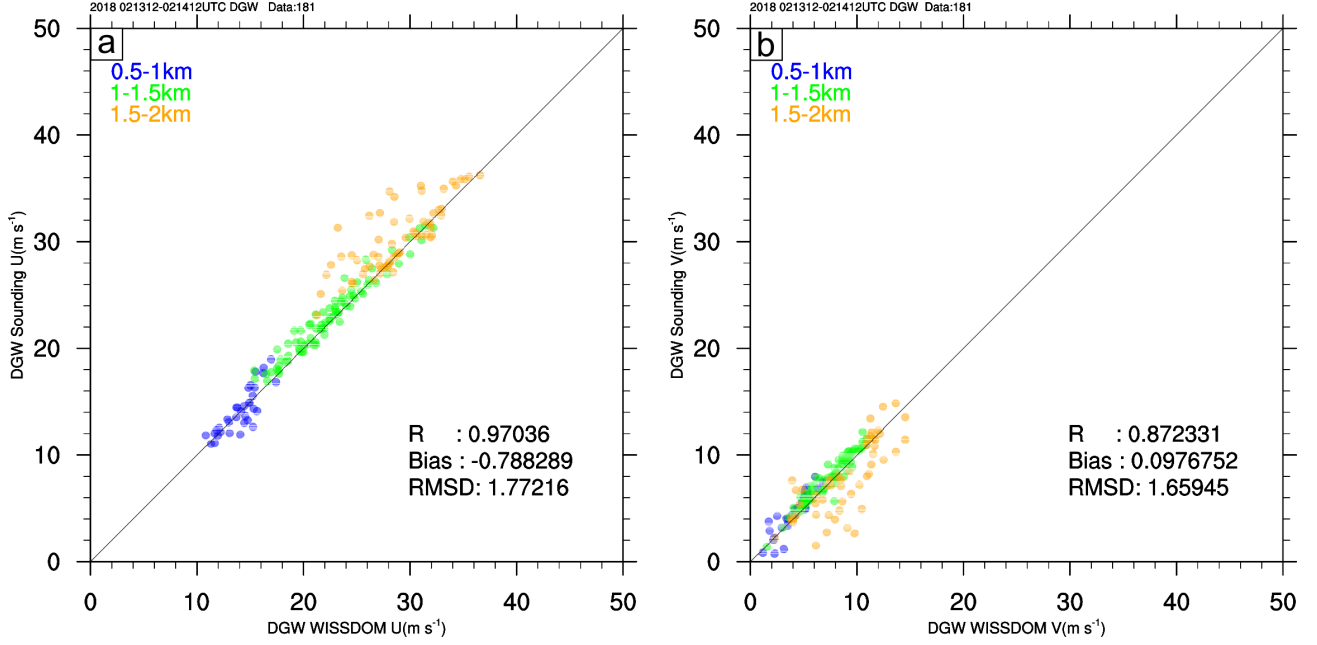
Figure. 6. Scatter plots of (a) u-component winds between the WISSDOM synthesis (x-axis) and sounding observations (y-axis) above the DGW site during the research period. The colors indicate different layers, and the numbers of data points, correlation coefficients, average biases and root mean square deviations are also shown in the figure. (b) The same as (a) but for v-component winds.

Overall, the u-component winds show a high correlation coefficient (exceeding 0.97), low average bias (-0.78 m s^{-1}), and the root mean square deviation (RMSD) of 1.77 m s^{-1}. The correlation coefficient of the v-component is also high (0.87), the average bias is 0.09 m s^{-1}, and the RMSD is 1.65 m s^{-1}.

467
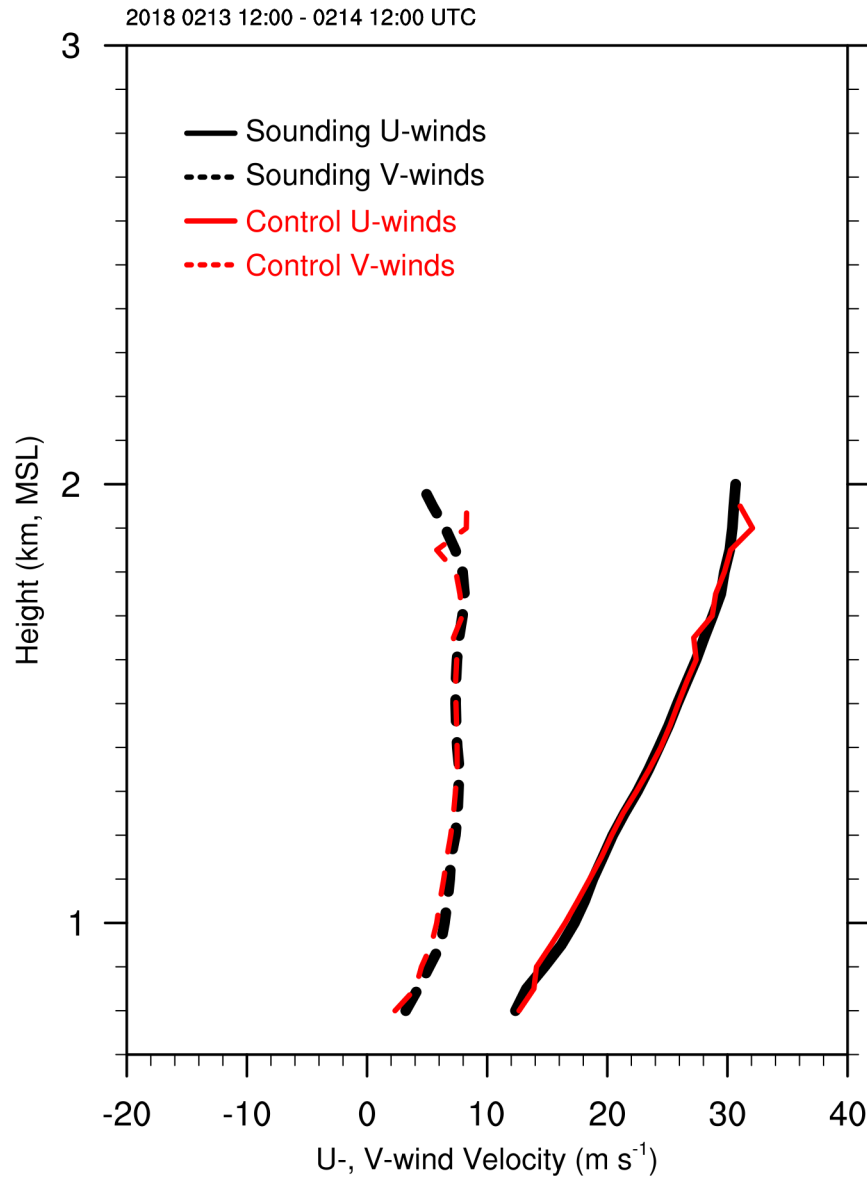
468 Figure 7. Vertical wind profiles of average horizontal winds derived from the WISSDOM synthesis (red lines and

469   vectors) and sounding observations (black lines and vectors) above the DGW site from 12:00 UTC on 13 to

470   12:00 UTC on 14 Feb. 2018. Solid lines indicate u-component winds (m s^{-1}), and dashed lines indicate v-

471   component winds (m s^{-1}).

472   The vertical profiles of the averaged u- and v-component winds for the period of 12:00 UTC

473 on 13 to 12:00 UTC on 14 Feb. 2018 is shown in Fig. 7 for the WISSDOM synthesis (red) and

474 sounding observations (black) launched from the DGW site. The average profiles agree well

475 except for the height above 1.5 km MSL, slight discrepancies of u- and v-component winds (< 1

476 m s^{-1}). Their statistical errors during the entire research period were quantified by the box plot

477 shown in Fig. 8.

478   The maximum difference in wind directions between the WISSDOM synthesis and sounding

479   observations is small at all layers. Except for relatively larger IQR existed (between ~−5 and 5

480   degrees) and larger median values (between ~0 and 5 degrees) can be found at the lowest level,

481   the interquartile range (IQR) and median values of the wind direction differences are smaller

482   (between ~0 and 2.5 degrees) during the entire research period (Fig. 8a). Basically, the IQR and

483   median values of the wind direction differences are close to 0 degrees above 1 km MSL. Fig. 8b

484   shows the difference in wind speed between the WISSDOM synthesis and sounding observations.

485   The differences of wind speed derived from WISSDOM was slightly underestimated in the layers

486   between ~0.85 and 1.3 km MSL. The median values of the wind speed differences were between

487   −1 and 0.5 m s^{-1}, and the IQR of wind speed differences was between −2 and 0.5 m s^{-1}. Above

488   1.3 km MSL, the differences in wind speed are small as their median values are close to 0 m s^{-1}.

489
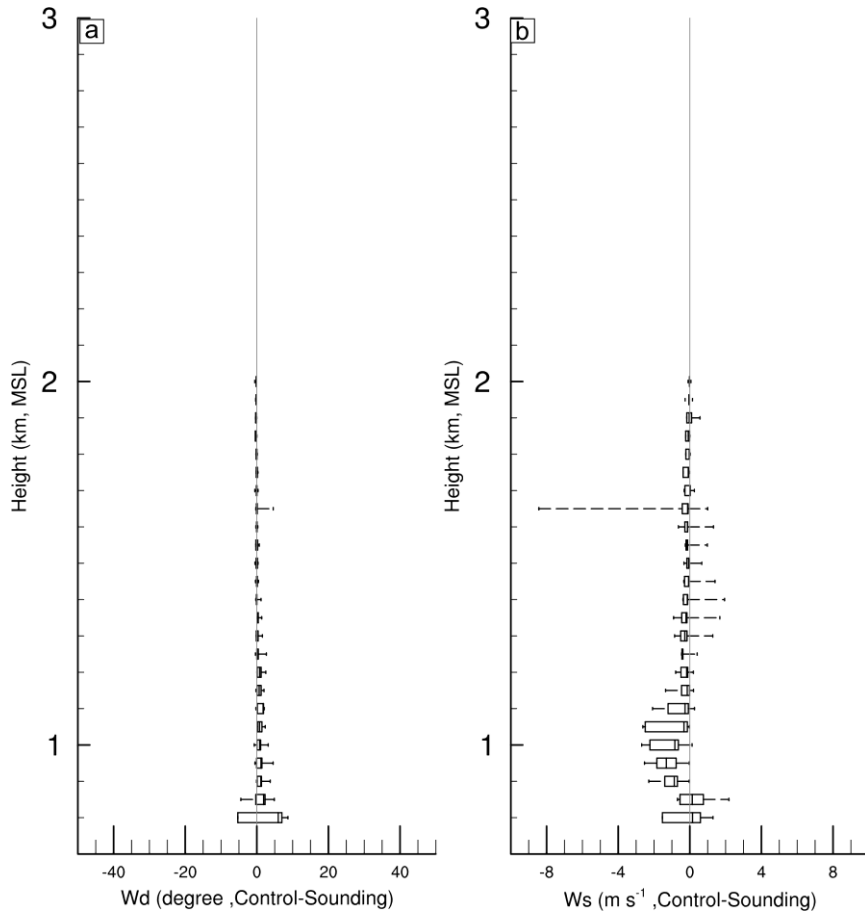
490

491   Figure 8. The box plot of average (a) wind direction discrepancies between the WISSDOM synthesis and sounding

492   observations above the DGW site during the research period. (b) Same as (a) but for the wind speed.

4.2.3 Lidar QVP

The lidar QVP is another observational reference used to evaluate the performance of derived winds from the WISSDOM synthesis. The scatter plots of the horizontal winds derived from WISSDOM and lidar QVP at the DGW site are shown in Fig. 9. The strength of the u-component winds increases with height in the range between approximately 10 m s^{-1} and 40 m s^{-1} from the surface up to ~2.5 km MSL (Fig. 9a). Although the results show a relatively high correlation coefficient (0.84) for the u-component winds from lower to higher layers in the entire research period, the degree of scatter is larger than that in Fig. 6a. The average bias and RMSD of the u-component winds are 2.83 m s^{-1} and 3.69 m s^{-1}, respectively. The correlation coefficient of v-component winds is lower (0.35) in association with low wind speed (<15 m s^{-1}) from the surface to 2.5 km MSL (Fig. 9b), and it may possibly relate to less coverages from lidar QVP data at higher layers. The average bias and RMSD of the v-component winds are 2.26 m s^{-1} and 2.92 m s^{-1}, respectively. The results of these scatter plot analyses are summarized in Table 2. Basically, the u-component winds have high correlations, relatively lower bias, and lower RMSD than the v-component winds because the environmental winds are more westerly.
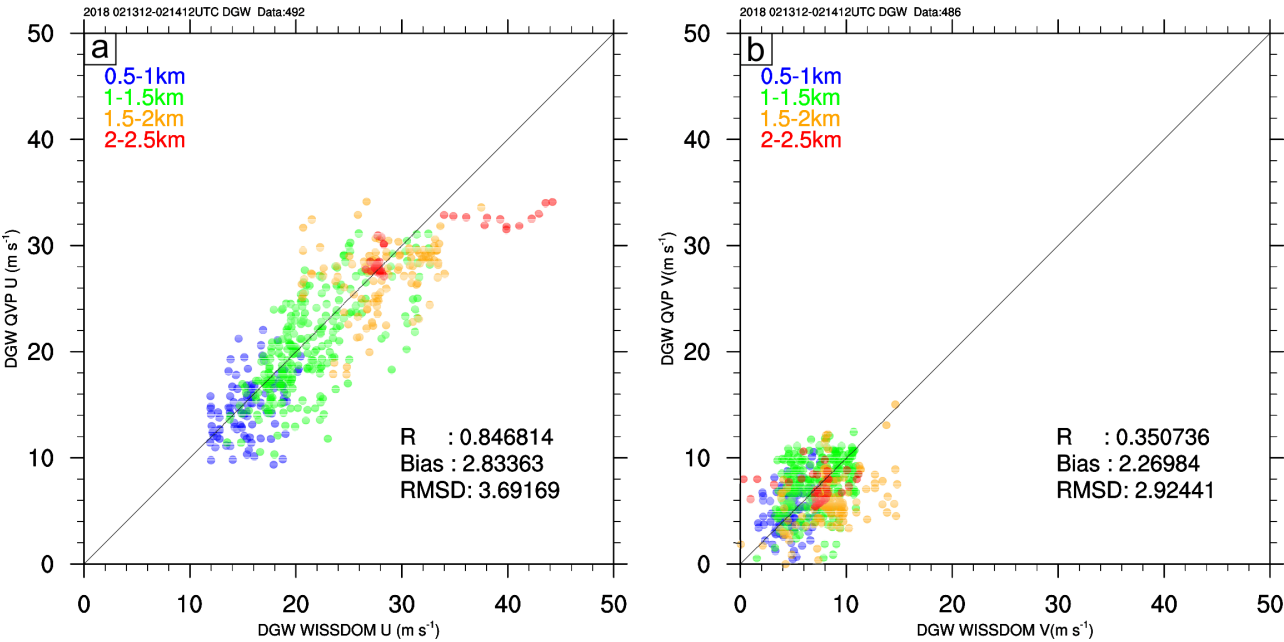
Figure 9. The same as Fig. 6 but for (a) u-component winds between the WISSDOM synthesis (x-axis) and lidar QVP (y-axis). (b) The same as (a) but for v-component winds.

511

Table 2 Summary of the intercomparisons between WISSDOM and observations

		Correlation coefficient	Average bias (m s^{-1})	RMSD (m s^{-1})
WISSDOM-sounding	u-component	0.97	-0.78	1.77
	v-component	0.87	0.09	1.65
WISSDOM-lidar QVP	u-component	0.84	2.83	3.69
	v-component	0.35	2.26	2.92

512   Compared to the sounding observations, additional w-component winds are available in

513 lidar QVP, which allows us to check their discrepancies in 3D winds. However, most of the

514 vertical velocity observations were quite weak (approximately ±0.2 m s^{-1}) above the DGW site,

515 and relatively low reliability of the derived vertical velocity could be expected in this event.

516 Therefore, the average vertical profiles of 3D winds were utilized to qualitatively check the

517 discrepancies between WISSDOM synthesis and lidar QVP during the research period (Fig. 10).

518 The results show that the average u-component winds have relatively smaller discrepancies

519 (approximately <1 m s^{-1}) between the WISSDOM synthesis (marked as WISS-U in Fig. 10) and

520 lidar QVP (marked as QVP-U) below ~1.3 km MSL at the DGW site. In contrast, there were

521 larger discrepancies (approximately >2 m s^{-1}) between 1.3 km and 2 km MSL. The average v-

522 component winds derived from WISSDOM (marked as WISS-V) and lidar QVP (QVP-V) were

523 generally weak, and the ranges of WISS-V and QVP-V were between ~2 m s^{-1} and 8 m s^{-1}.

524 Generally, the vertical profiles of WISS-V were nearly overlain with QVP-V, and their

525 discrepancies existed in the height range 1.6~2.0 km MSL (maximum ~4 m s^{-1}). Smaller (larger)

526 discrepancies of w-component winds were significantly below (above) the height at ~1.3 km

527 MSL (maximum discrepancies ~0.6 m s^{-1} at 1.7 km MSL). Despite the larger discrepancies, the

528 similar patterns of W can also be shown. In summary, the discrepancies in the 3D winds between

529 the WISSDOM synthesis and lidar QVP were small in the lower layers and large in the higher

530 layers because the observational data from lidars and AWS provided good quality and sufficient

531 wind information at the lower layers but not in the higher layers (lower coverages of lidar data

532   above 1.3 km MSL, cf. Fig. 4).

533
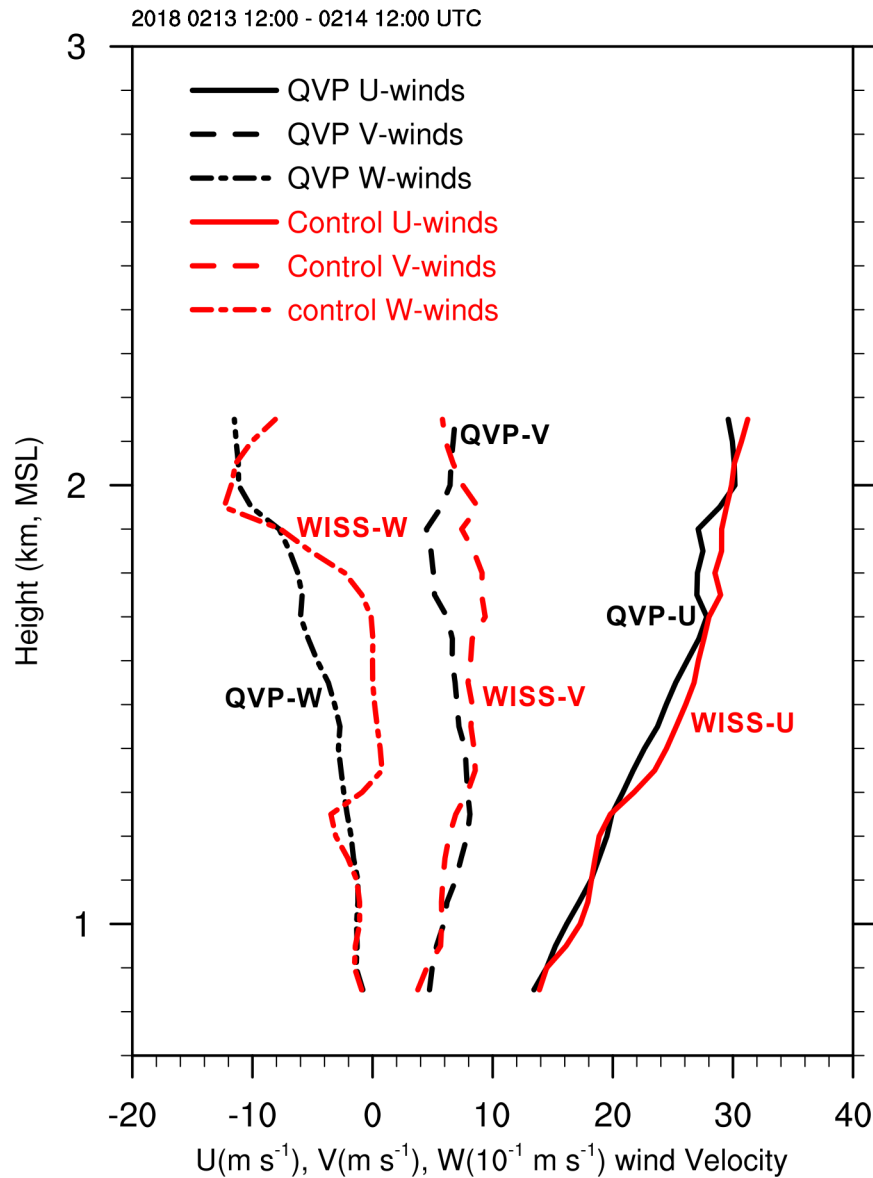
Figure 10. Vertical wind profiles of average 3D winds derived from the WISSDOM synthesis (red lines and vectors)
and lidar QVP (black lines and vectors) above the DGW site from 12:00 UTC on 13 to 12:00 UTC on 14 Feb.
2018. Solid lines indicate u-component winds (m s^{-1}), dashed lines indicate v-component winds (m s^{-1}), and
dash-dotted lines indicate w-component winds ($1×10^1$ m s^{-1}). The u-, v-, and w-component winds derived from
the WISSDOM synthesis (lidar QVP) were marked by WISS-U (QVP-U), WISS-V (QVP-V), and WISS-W
(QVP-W), respectively.

540   Fig. 11 shows the quantile distribution of statistical errors of wind direction, wind speed and

541   vertical velocity between the WISSDOM synthesis and lidar QVP during the research period.

542   The IQR of the wind direction is smaller (−5~5 degrees) in the layers from 0.85 km to 1.5 km

543   MSL and turns to approximately −10~0 degrees above 1.5 km MSL. The median values of wind

544   direction are smaller −5~5 degrees) from near the surface to the upper layers (Fig. 11a). Fig. 11b

545   shows that the median values (IQR) of wind speed are approximately –1~1 m s^{-1} (–2~2 m s^{-1})

546   below 1.5 km MSL, and they all become larger with heights above 1.5 km MSL (between −1 and

547   3 m s^{-1} for median values and −4~4 m s^{-1} for the IQR). The statistical error of the vertical velocity

548   reveals that the IQR is −0.2~0.2 m s^{-1} (−0.8~0.8 m s^{-1}) below (above) 1.3 km MSL, and the

549   median values are 0~0.2 m s^{-1} −0.2~0.6 m s^{-1}) below (above) 1.3 km MSL. The results of

550   statistical errors are summarized in Table 3.

551

552
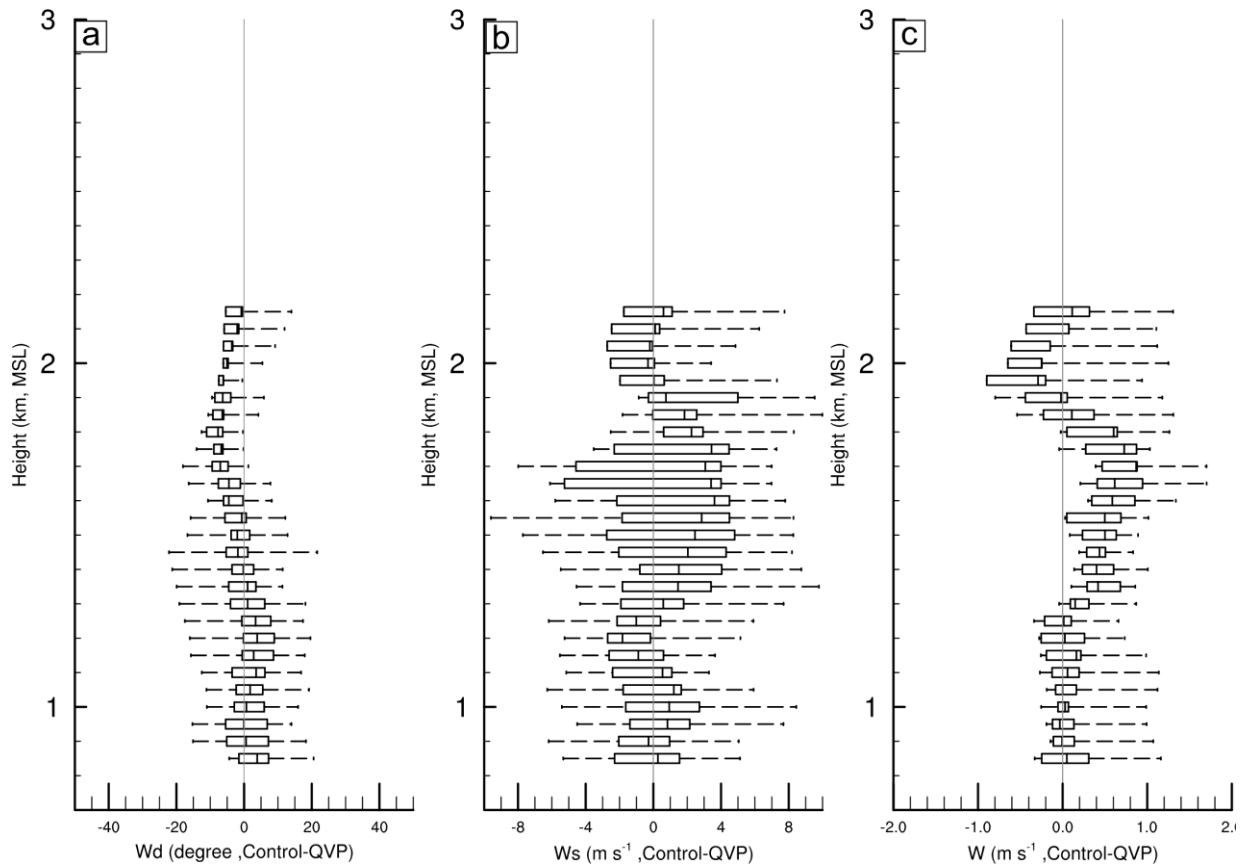
553   Figure 11. The box plot of average (a) wind direction discrepancies between the WISSDOM synthesis and sounding

554   observations above the DGW site during the research period. (b) Same as (a) but for the wind speed. (c) Same

555   as (a) but for the w-component winds.

556

Table 3   Summary of the statistical errors between WISSDOM and observations

		Interquartile range (IQR)	Median values
WISSDOM-sounding	wind direction	0~2.5 (deg.)	0~2.5 (deg.)

	wind speed	−2~0.5 (m s^{-1})	−1~0.5 (m s^{-1})
	wind direction	−10~5 (deg.)	−5~5 (deg.)
WISSDOM-lidar QVP	wind speed	-4~4 (m s^{-1})	−1~3 (m s^{-1})
	w-component winds	−0.8~0.8 (m s^{-1})	−0.2~0.6 (m s^{-1})

5. Sensitivity test with various datasets, data implementation and weighting coefficients

5.1 Impacts of various datasets (Experiment A)

In this session, the impacts of various datasets implemented in the WISSDOM synthesis were evaluated, then the range of errors can be estimated from each independent observation. The basic setting of Experiment A took off several inputs from the WISSDOM control run (cf. Table 1) as four designs in Experiment A. The details of these four designs are summarized in Table 4 as the control run without the lidar observations (A-1), the control run without the AWS observations (A-2), the control run without the sounding observations (A-3) and the control run without the LDAPS data (A-4). The discrepancies of 3D winds were examined between the control run and each design in Experiment A. Since the environmental wind speed is nearly comprised of uniform westerlies in this event, the results only show the difference in u-component winds between control run and each design (A-1~A-4) in Fig. 12. In addition, to evaluate the performances between the modified WISSDOM and original version by using Doppler lidar data, additional test was designed as only Doppler lidar data are used without additional constraints from J_6 ~ J_8 (A-5).

Fig. 12a reveals the discrepancies in horizontal u-component winds at 800 m MSL as the A-1 is subtracted from the control run. This result reflects the impacts of lidar observations on the u-component winds in the WISSDOM synthesis. The most significant contributions from the

lidar observations are the high wind speed existing near the DGW site in a relatively narrow

valley. The mechanisms of the accelerated wind speed due to the channeling effect in this local

area were verified by our previous study (Tsai et al. 2022). The lidar observations also contributed

to the high wind speed in another area near the western side of the MHS site (128.68°E, 37.66°N).

Based on the analysis in the vertical cross section of u-component winds in A-1 (Fig. 12b), the

lidar observations significantly affected the high wind speed only in the lower levels (below ~900

m MSL) but not in the higher levels. Lidar observations provided sufficient coverage only for

lower levels and not higher levels (cf. Fig. 4).

Table 4 Experiment setting (sensitivity testing)

	Various datasets	Including Doppler lidars, AWS, Soundings, LDAPS
Control run	Interpolation of AWS	RI: 1.0 km, VE: 90%
	Weighting Coefficient	Doppler Lidars (α_1): 10^6 Background (α_2): 10^2 Sounding (α_6): 10^6 AWS (α_7): 10^6 LDAPS (α_8): 10^3
Experiment A	Various datasets	A-1 Excluding Doppler Lidars A-2 Excluding AWS A-3 Excluding Soundings A-4 Excluding LDAPS A-5 Only Doppler lidars
Experiment B	Interpolation of AWS	B-1 RI: 0.5 km, VE: 50% B-2 RI: 0.5 km, VE: 90% B-3 RI: 1.0 km, VE: 50% B-4 RI: 2.0 km, VE: 50% B-5 RI: 2.0 km, VE: 90%
Experiment C	Weighting Coefficient (constraints)	C-1 AWS (α_7): 10^3 C-2 Doppler Lidars (α_1): 10^3 C-3 LDAPS (α_8): 10^6

The impacts of the AWS cause negative values on the u-component winds in most areas at

800 m MSL in A-2 (Fig. 12c), especially in the western areas of the MHS site. Negative

587 contributions of the u-component winds produced by the AWS observations were restricted near

588 the surface, and the low wind speed area was extended to ~100 m above the surface (Fig. 12d).

589 The contributions of the u-component winds from the sounding observations were weak near the

590 DGW sounding site in A-3 (Figs. 12e and 12f). The impacts of u-component winds from the

591 LDAPS datasets were rather smaller in most of analysis area. in A-4 (Figs. 12g and 12h).

592 Relatively weak winds were presented from the results of A-5 (Figs. 12i and 12j), especially at

593 the lower layers. These results reflects that relatively stronger winds were retrieved when

594 additional constraints are removed. Furthermore, it is also implied that the retrieved winds can

595 be reasonably adjusted in the modified version of WISSDOM.

596
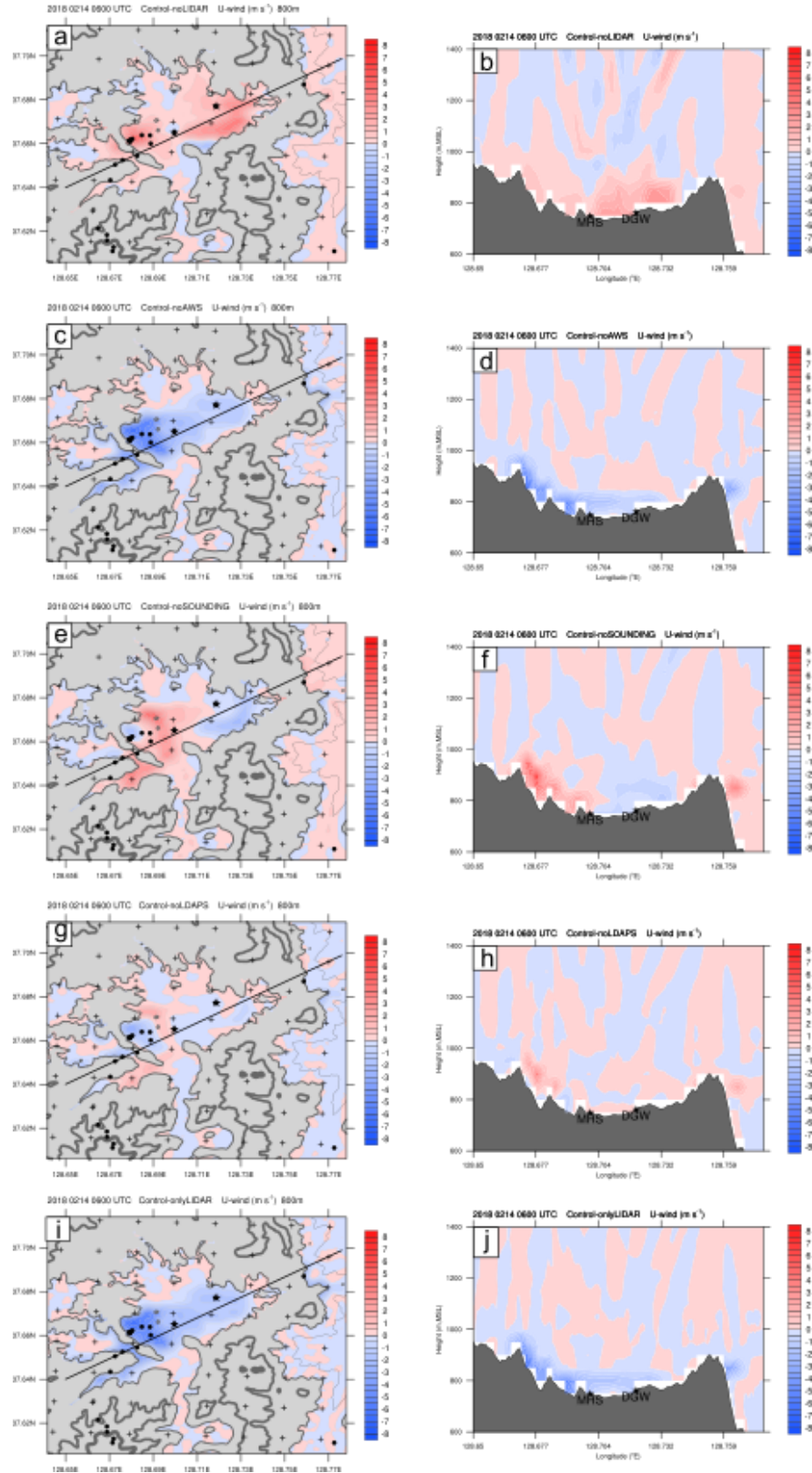
597   Figure 12. (a) The discrepancies in horizontal u-component winds between the control run and A-1 at 800 m MSL

598   at 06:00 UTC on 14 Feb. 2018. (b) The same as (a) but for the vertical section along the black line in (a). (c) and

599   (d) are the same as (a) and (b) but for A-2. (e) and (f) are the same as (a) and (b) but for A-3. (g) and (h) are the

600   same as (a) and (b) but for A-4. (i) and (j) are the same as (a) and (b) but for A-5.

601

602   Averaged discrepancies of derived 3D winds for each vertical level are shown in Fig. 13.

603   These results summarized a series of sensitivity tests if the WISSDOM synthesis lacks certain

604   data inputs (i.e., A-1~A-4 in Experiment A) for derived u-, v- and w-component winds in the test

605   domain. Overall, the maximum absolute value of averaged discrepancies for Experiment A are

606   smaller than approximately 0.5 m s^{-1}, which are the discrepancies of the u-component winds for

607   A-1 and A-2 located at 800 m MSL. Except for these values, the values of the derived u-, v- and

608   w-component winds for A-1~A-2 are approximately smaller than 0.2 m s^{-1} from the surface up

609   to the top in the test domain. Based on the results of A-5, relatively stronger values of derived u-

610   component (exceeded −0.4 m s^{-1} at lower layers) can be obtained from the setting like old version

611   of WISSDOM. The wind speed can be better modulated in modified version of WISSDOM when

612   the Doppler lidar observations were adopted. These results also implied that the ranges of errors

613   are relatively small when we try to evaluate the discrepancies between the control run and each

614   independent observation. In summary, the results of this experiment (cf. Fig. 13) concluded that

615   the lidar and AWS data are more critical inputs in modified WISSDOM, and it will be benefits if

616   more inputs can be included.

617
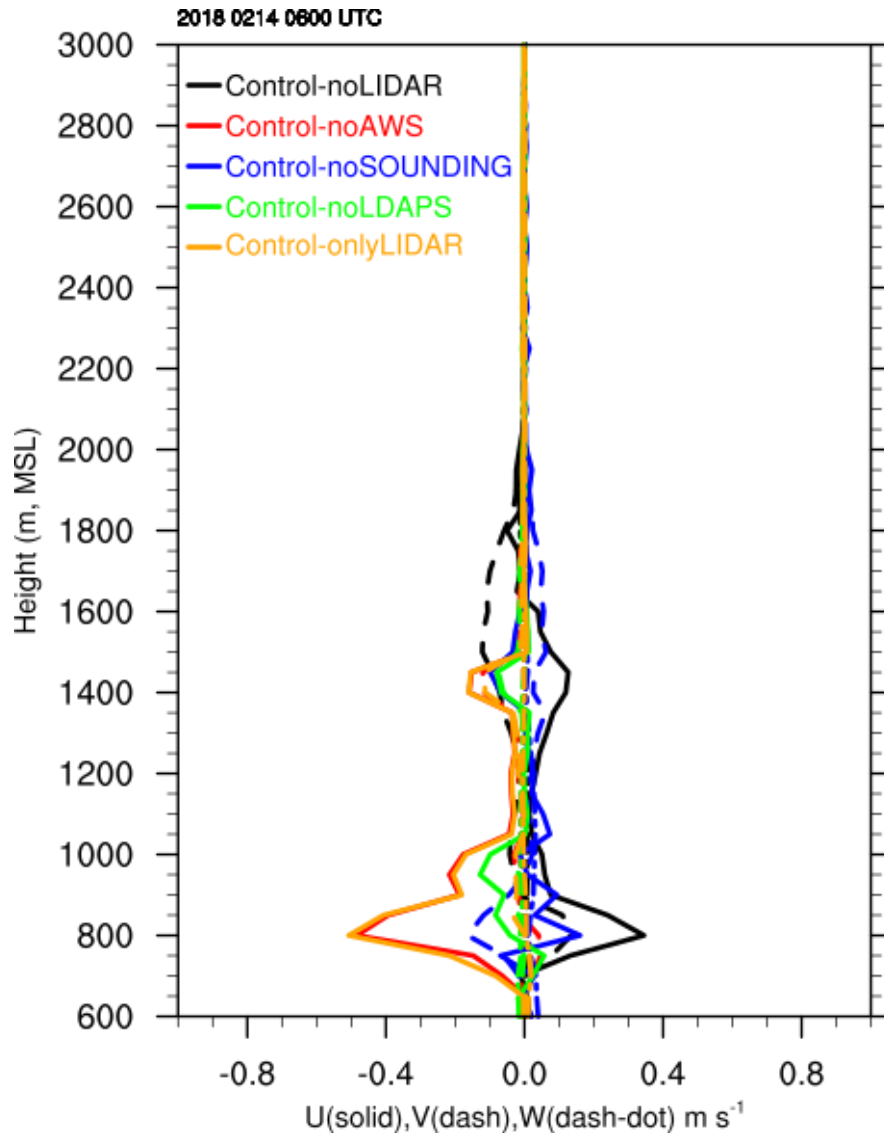
618   Figure 13. Vertical profiles of averaged discrepancies of 3D winds for each design in Experiment A at 06:00 UTC

619   on 14 Feb. 2018. The averaged discrepancies of u-, v- and w-component winds were plotted by solid, dash, and

620   dash-dot lines, and the black, red, blue, green and orange lines indicate A-1, A-2, A-3, A-4 and A-5, respectively.

621   **5.2 Radius of influence (RI) and vertical extension for the AWS (Experiment B)**

622   Experiment B was performed to check the discrepancies in 3D winds between the control run

623   and the different settings of RI and VE with the AWS observations. There were five designs (B-

624   1~B-5) in Experiment B with the ranges of RI (VE) between 0.5 km (50%) and 2 km (90%).

625   Because the average distance between each AWS site is approximate from 0.1 to 2 km and more

626   data can be included in vertically. The details are shown in Table 4. The horizontal u-component

627   winds at 800 m MSL and the vertical structure of Experiment B at one time step (06:00 UTC on

628   14 February 2018) are shown in Fig. 14. An unusual circular area with positive discrepancies

629   around the MHS site was depicted in B-1 (Figs, 14a and 14b), which may have been produced

630   by the insufficient RI distance and VE (unusual circle can be vanished when VE becoming 90%).

631   Relatively smaller RI and VE values can only include relatively less wind information if the

632   distances are large between each AWS station. Enlarging the RI and VE are required to

633   appropriately include more wind information from the AWS observations. Figs. 14c and 14d

634   show the results of B-2 as VE reached 90%. Although the unusual circle vanished, there were

635   discontinuities with negative values near the northern and southern areas of the MHS site and

636   positive areas surrounding the AWS (128.68°E, 37.66°N). The setting of B-3 was similar to that

637   of the control run except that the VE was 50%. The discrepancies were relatively small, albeit

638   dense AWS stations contributed even smaller negative values in the western areas of the MHS

639   sites (Figs. 14g and 14h). Obviously, positive discrepancies appeared near the northern and

640   southern areas of the MHS site in B-4 and B-5 (Figs. 14g-j). The impacts of the AWS with various

641   settings (B-1~B-5) on the discrepancies in u-component winds were both restricted near the

642   surface, even with a larger RI and high VE.

643
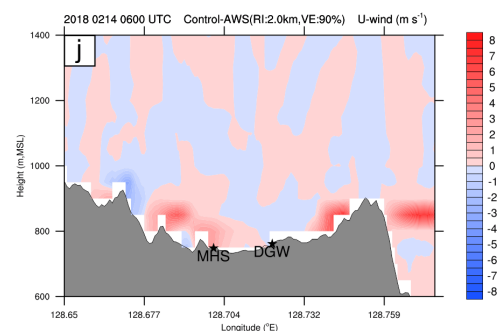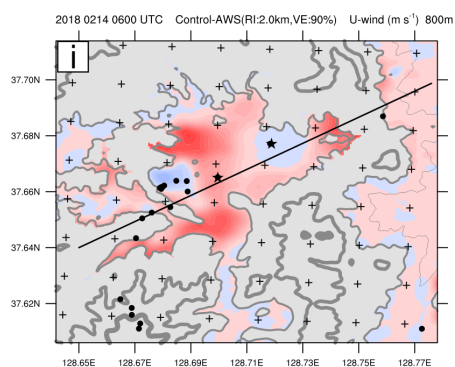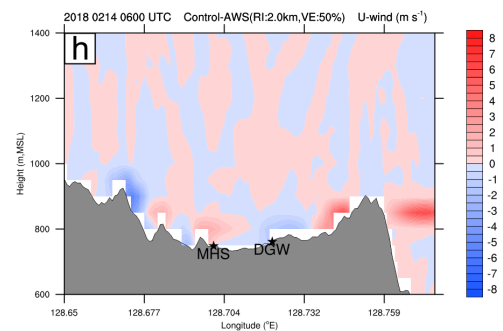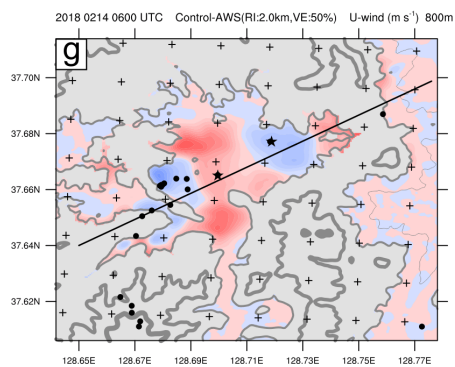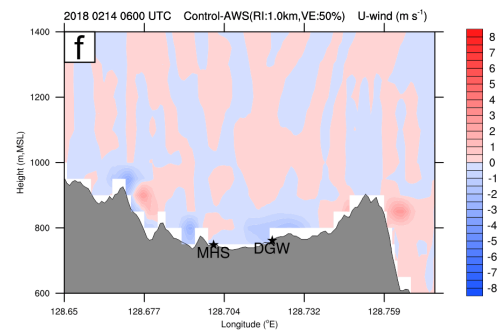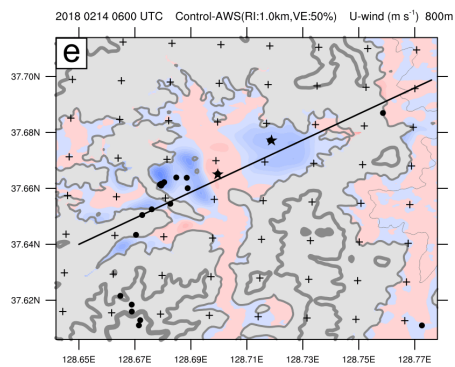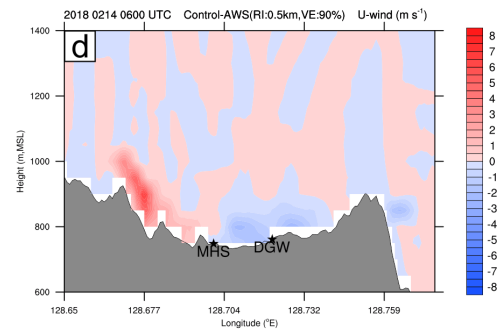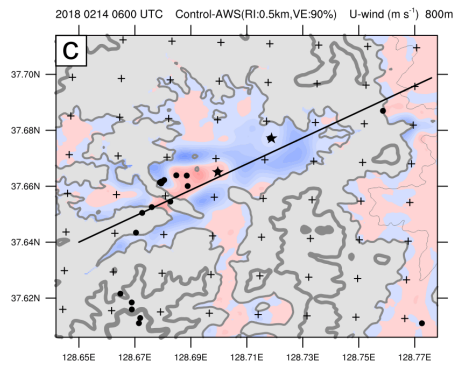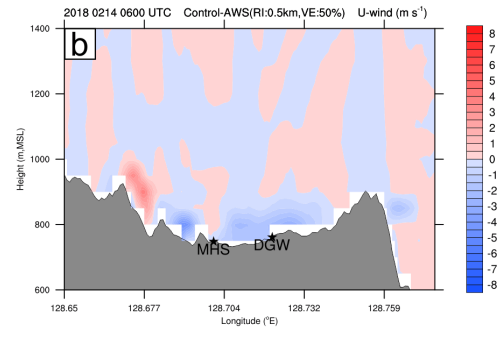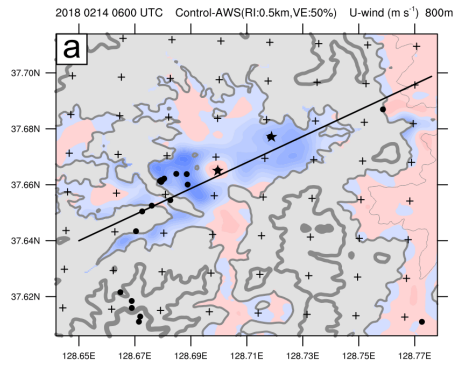
644 Figure 14. The same as Fig.12, but (a) and (b) for B-1. (c) and (d) are the same as (a) and (b) but for B-2. (e) and (f)

645   are the same as (a) and (b) but for B-3. (g) and (h) are the same as (a) and (b) but for B-4. (i) and (j) are the same

646   as (a) and (b) but for B-5.

647   Fig. 15 shows the vertical profiles of averaged discrepancies of derived 3D winds in

648 Experiment B. This figure summarizes the results of sensitivity testing with different settings of

649 the RI and VE in WISSDOM (i.e., B-1~B-5 in Experiment B, shown in Table 4) for derived u-,

650 v- and w-component winds in the test domain. The maximum discrepancies of u-component

651 winds in B-1, B-2 and B-3 were quite small at only 0.4, 0.3 and 0.2 m s^{-1}, respectively.

652 Nevertheless, the maximum discrepancies of u-component winds for B-4 and B-5 were larger

653 than 0.6 m s^{-1} and even exceeded ~1 m s^{-1}. Although the discrepancies in the u-component winds

654 in B-1 were small, the discrepancies in the v-component winds in B-1 reveal unusual patterns,

655 with larger positive values at ~1100 m MSL and negative values at ~1800 m MSL (black dashed

656 line in Fig. 15), the possible reason is the minimizations of cost function are not converged well

657 because relatively few and weak v-component winds were included in B-1. Except for this value,

658 the maximum discrepancies of v-component winds were small for B-2~B-5, and the maximum

659 discrepancies of w-component winds were also small for all of Experiment B. Note that B-3

660 always has the smallest discrepancies with the derived 3D winds because the setting is quite

661 similar to the control run. The conclusions indicated that the moderate setting (i.e., RI is 1 km)

662 will be helpful to get the smallest differences with the control run. In addition, the wind directions

663 and speed should be more dominated by terrains at lower layers, the implements of AWS data

664 are very important for the modified WISSDOM synthesis, especially at the height below 900 m

665 MSL.

666
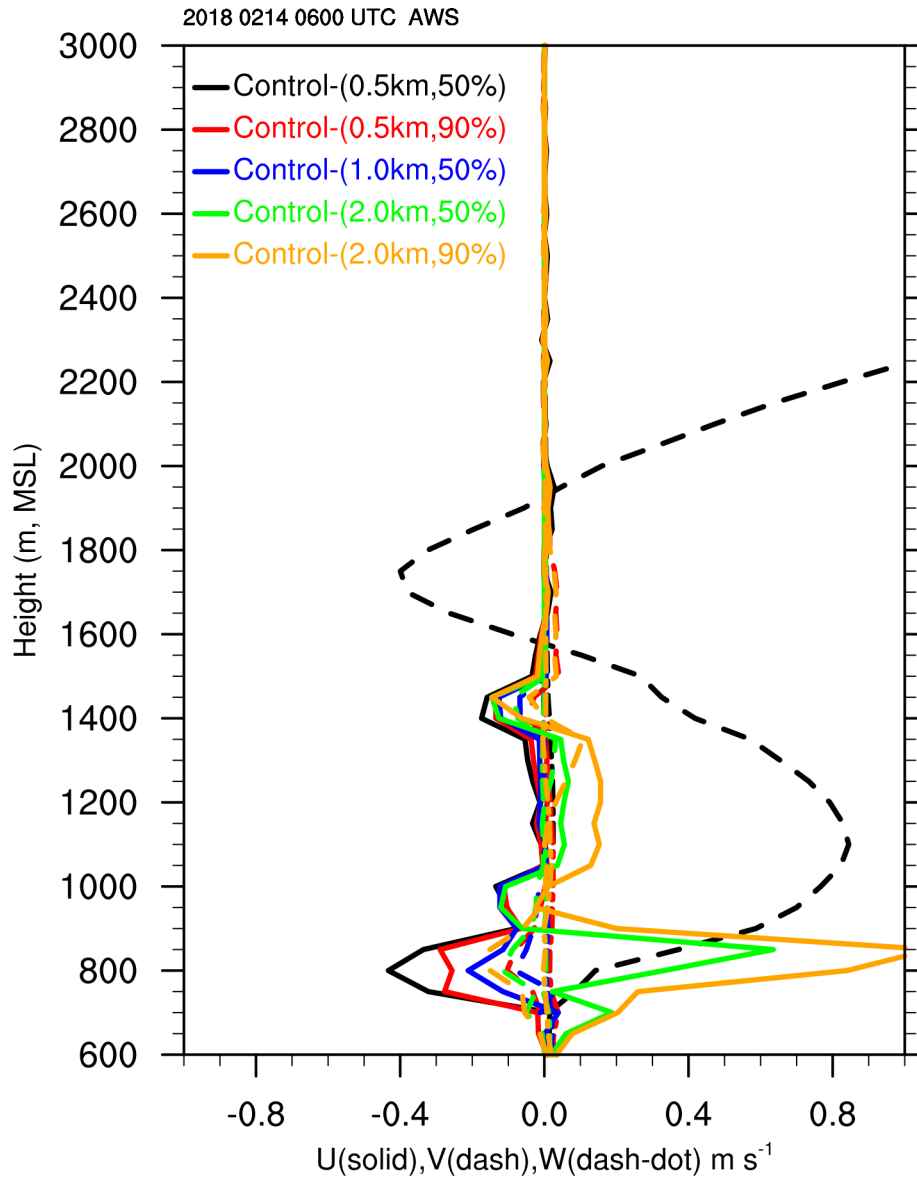
667   Figure 15. The same as Fig. 13. but for B-1~B-5.

5.3 Different weighting coefficients for the constraints (Experiment C)

669   Experiment C was designed to check the discrepancies in the derived u-component winds

670   between the control run and experimental runs with different weighting coefficients for each

671   constraint related to the AWS, lidar and LDAPS (corresponding to C-1, C-2 and C-3 in Table 4).

672   Originally, the weighting coefficients for the AWS and lidar observations were set to 10^6, and the

673   value was 10^3 for the LDAPS dataset (i.e., control run, Table 1). The results of Experiment C

674   show significant negative discrepancies in u-component winds near the surface in C-1, especially

675   in the areas next to the AWS (128.68°E, 37.66°N). The discrepancies for C-1 (Figs. 16a and 16b)

676   and C-2 (Figs. 16c and 16d) are similar to those for A-2 (Figs. 12c and 12d) and A-1 (Figs. 12a

677   and 12b), respectively. The inputs of AWS and lidar both contributed relatively weak impacts to

678   the WISSDOM synthesis when the weighting coefficient was set to 10^3. Irrational patterns were

679   depicted when the weighting coefficient of LDAPS inputs increased to 10^6, and larger and

680   positive discrepancies were crowded into most areas in the valley (i.e., C-3, Figs. 16e). Larger

681   and positive discrepancies existed only near the surface, and there were negative discrepancies

682   between approximately 1000 m and 1400 m (Fig. 16f). Note that the influences of sounding

683   observations also existed above the DGW site in scenario C-3.

684   The vertical profiles of averaged discrepancies of derived 3D winds in Experiment C are

685   shown in Fig. 17. Absolute values of the discrepancies in the u-, v- and w-component winds are

686   smaller than 1 m s^{-1}, except for the discrepancies in the v-component winds with low weighting

687   of the AWS observations (i.e., C-1) and the discrepancies in the u- and v-component winds with

688   the high weighted LDAPS (i.e., C-3). The discrepancies in the v-component winds in C-1

689   exceeded −5 m s^{-1} at ~1100 m MSL and were larger than −15 m s^{-1} above 2600 m MSL. These

690   unreasonable characteristics are also shown as the discrepancies in the v-component winds in B-

691   1 (cf. Fig. 15). The discrepancies in the u- and v-component winds in C-3 are 15 m s^{-1} and 4 m

692   s^{-1}, respectively, in the layers between 700 and 900 m MSL. Alternative positive and negative

693   discrepancies in the range of -3 to 3 m s^{-1} for the u-component winds in C-3 were found above

694   1000 m MSL. The conclusions reveals that the weights of the AWS and LDAPS (lidar) are (not)

695   too sensitive to the derived winds. Therefore, the weights of LDAPS and AWS are not necessary

696   changed too much.

697
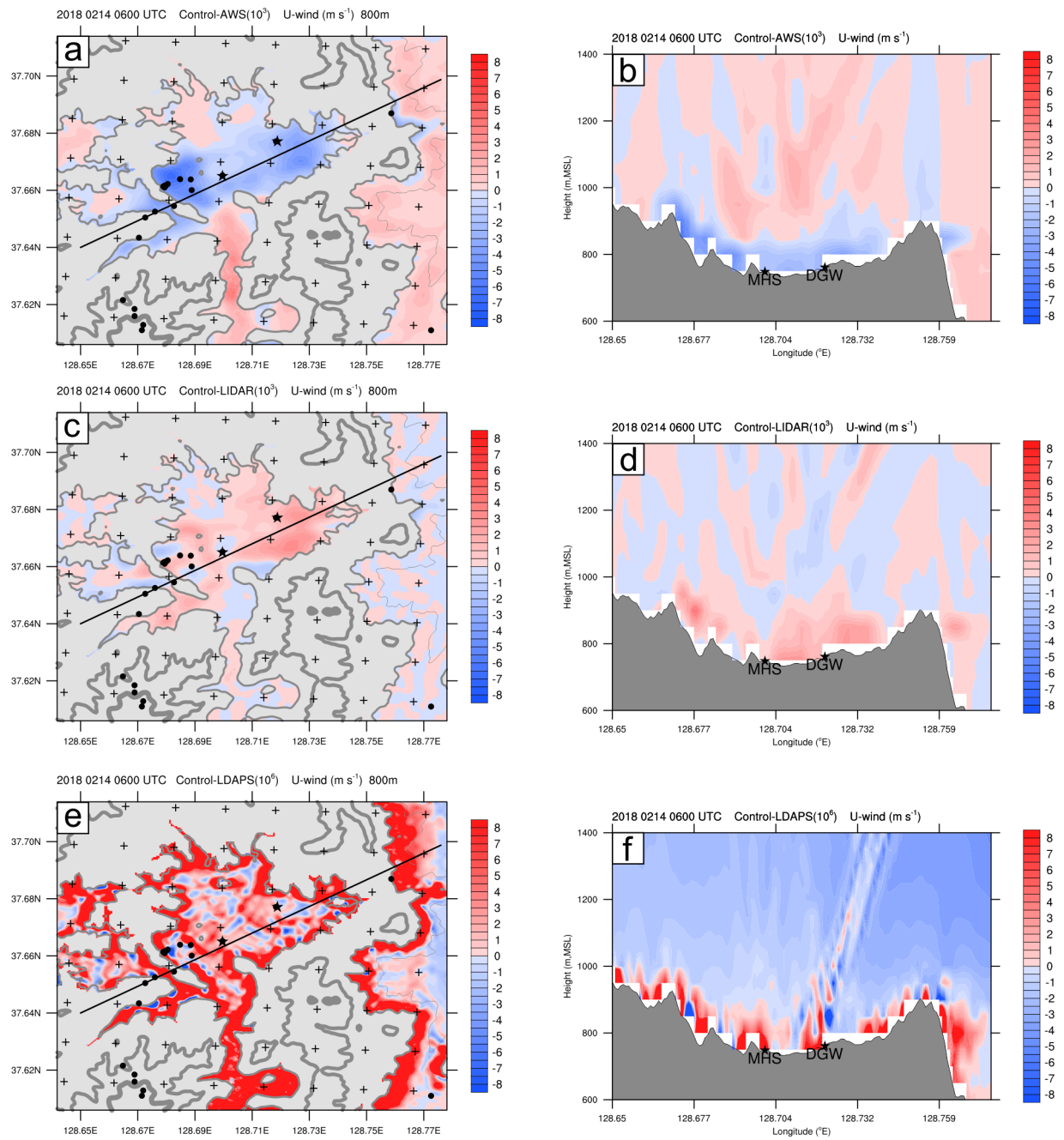
698   Figure 16. The same as Fig.12, but (a) and (b) for C-1. (c) and (d) are the same as (a) and (b) but for

699   are the same as (a) and (b) but for C-3.

700
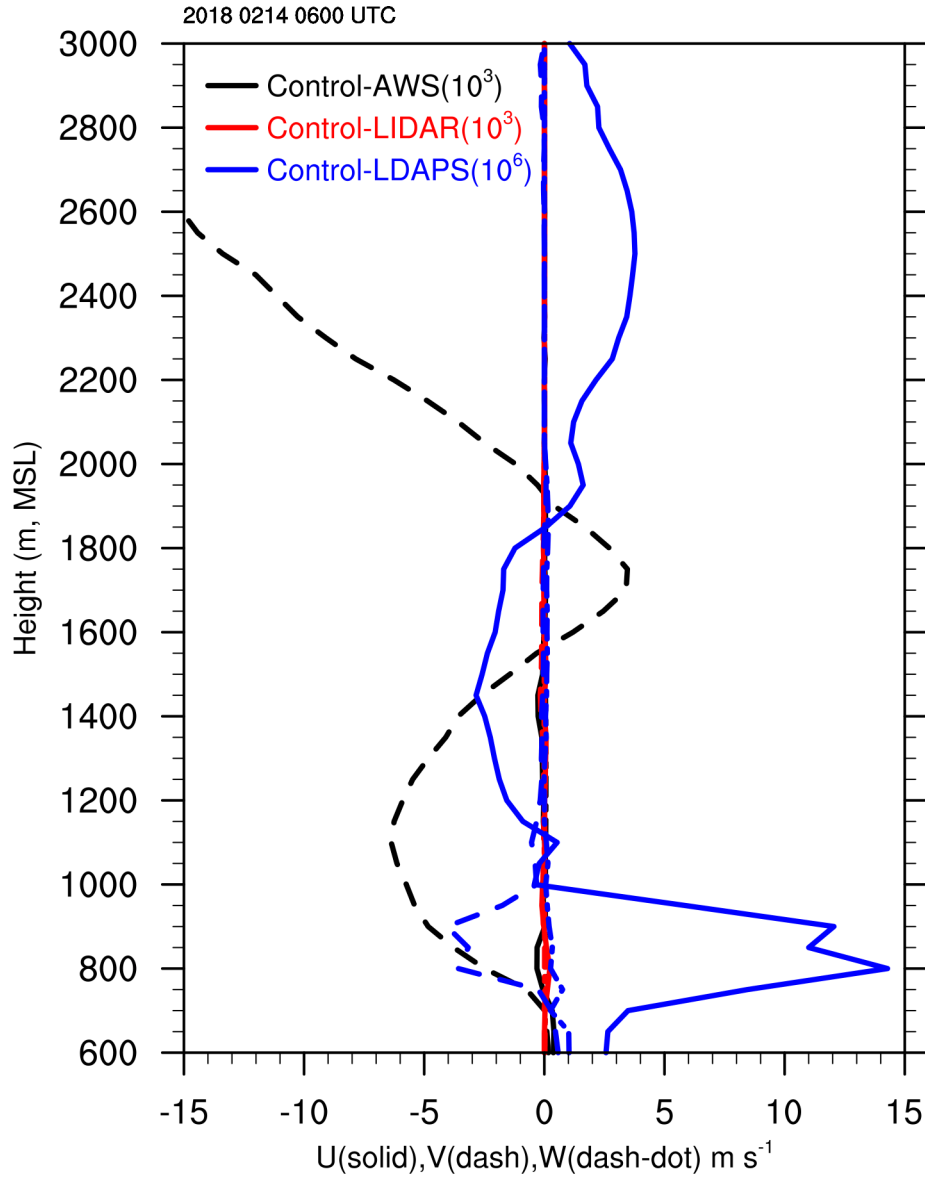
701 Figure 17. The same as Fig. 13 but for C-1~C-3.

6. Conclusion

703   A modified WISSDOM synthesis scheme was developed to derive high-quality 3D winds

704 under clear-air conditions. The main difference from the original version is that multiple lidar

705 observations were used, and high-resolution 3D winds (50 m horizontally and vertically) were

706 first derived in the modified WISSDOM scheme. In addition, all available datasets were included

707 as one of the constraints in the cost function in this study. The data implementation and the

708 detailed principles of the modified WISSDOM were also elaborated. This modified WISSDOM

709 scheme was performed over the TMR to retrieve 3D winds during a strong wind event during

710 ICE-POP 2018. The performance was evaluated via a series of sensitivity tests and compared

711 with conventional observations.

712   The intercomparisons of horizontal winds during the entire research period reveal a relatively

713 high correlation coefficient between the optimal results of WISSDOM synthesis and sounding's

714 u- (v-) component winds exceeding 0.97 (0.87) at the DGW site. Furthermore, the average bias

715 is -0.78 m s^{-1} (0.09 m s^{-1}), and the RMSD is 1.77 m s^{-1} (1.65 m s^{-1}) for the u- (v-) component

716 winds. The intercomparisons of 3D winds between the WISSDOM synthesis and lidar QVP also

717 showed a higher correlation coefficient (0.84) for u-component winds, but a relatively smaller

718 correlation coefficient remained at 0.35 for v-component winds in this strong wind event. The

719 average bias (RMSD) of u-component winds is 2.83 m s^{-1} (3.69 m s^{-1}), and the average bias and

720 RMSD of v-component winds are 2.26 m s^{-1} and 2.92 m s^{-1}, respectively (cf. Table 2). Chen

721 (2019) analyzed the correlations between 3D winds derived from radar and observations in

722 several typhoon cases; the mean correlation coefficient ranged from 0.56 to 0.86, and the RMSD

723 was between 1.13 and 1.74 m s^{-1}. Compared to their results, only u-component winds have

724 relatively higher correlation coefficients, but the RMSD values are slightly higher in this study,

725 which may have been caused by the high variability in westerly winds associated with the moving

726 LPS. The statistical error results of the winds between the optimal results of WISSDOM synthesis

727 and observations show a good performance of the retrieved 3D winds in this strong wind event

728 (Table 3). Generally, the median values of wind directions are within ~10 degrees. Compared

729 with lidar QVP (sounding observations) the median values of the wind speed are approximately

730 -1~3 m s^{-1} (-1~0.5 m s^{-1}) and the vertical velocity is within -0.2~0.6 m s^{-1}. Compared with

731 lidar QVP (sounding observations) above the DGW site, the interquartile range of wind directions

732 is -10~5 (0-2.5) degrees, the wind speed is approximately -4~4 m s^{-1} (-1~3 m s^{-1}) and the

733 vertical velocity is -0.8~0.8 m s^{-1}. The summaries of correlation coefficients, average bias, the

734 RMSD, and the range of statistical errors are show in the schematic diagrams as Figs. 18a and

735   18b.
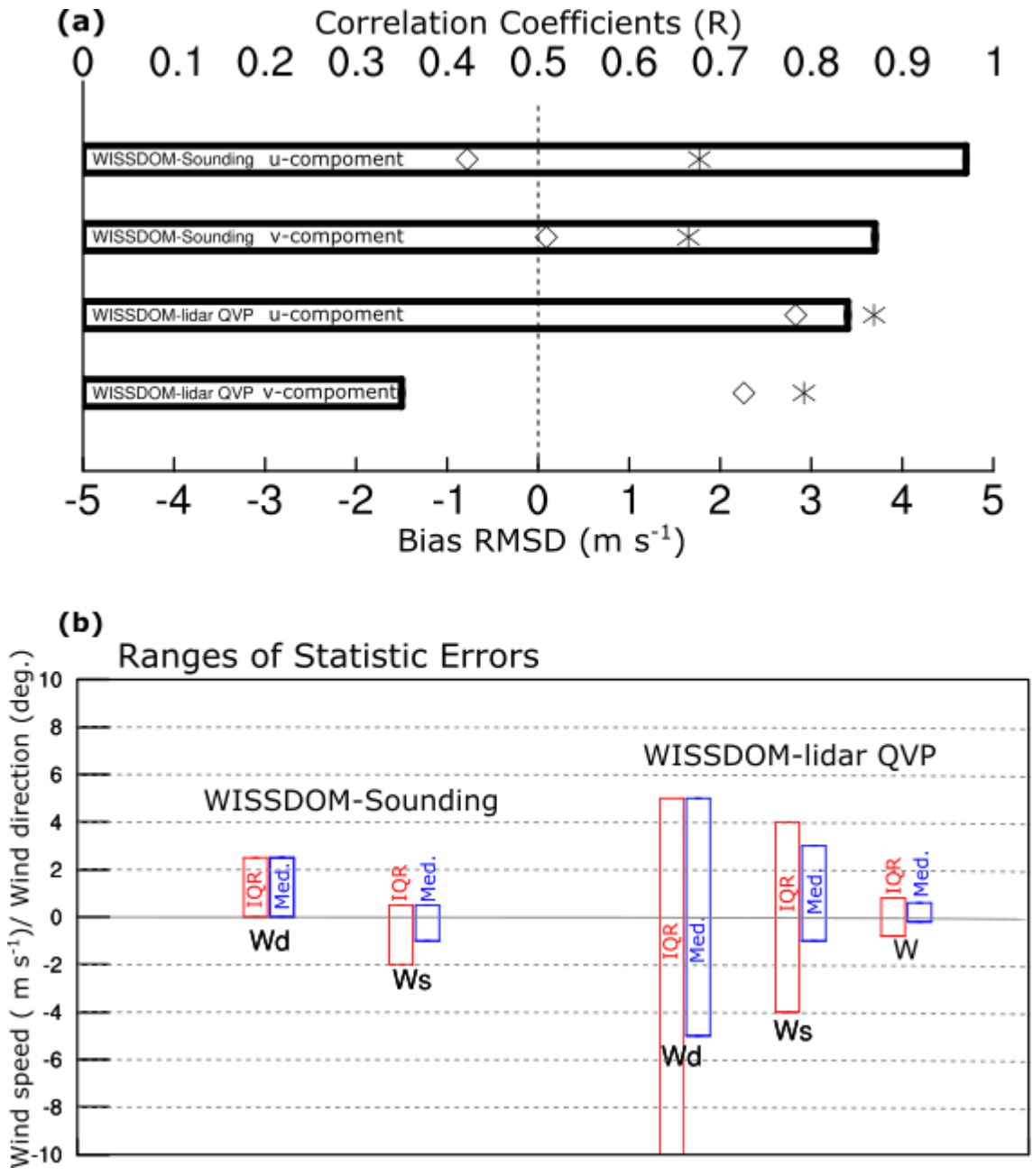
Figure 18. Schematic diagrams for the results of intercomparisons on (a) the correlation coefficients (R, histograms),
      the average bias (marked as diamonds), and the RMSD (marked as asterisks). (b) The ranges of statistic error for
      the IQR (red boxes) and median values (blue boxes). The wind directions and wind speed are denoted as Wd and
      Ws, respectively.

741   A control run (see the basic setting in Table 1) was set to explore the importance of acquired

742   observation datasets, various distances of RI, VE from the AWS observations, and the weighting

743   coefficient for each constraint (i.e., Experiments A-C, Table 4). The results of Experiment A

744   show that the lidar and AWS play critical roles in the derived horizontal winds, and the lidars

(AWS) provided positive (negative) contributions in stronger (weaker) wind speeds near the surface. The sounding and the LDAPS provided relatively smaller impacts on the derived horizontal winds from the WISSDOM synthesis. In Experiment B, the smallest discrepancies in 3D winds were depicted when the RI (VE) was set to 1 km (50%); it indicated that the optimal setting of the RI is 1 km. However, there were larger discrepancies in 3D winds (from -0.4 m s^{-1} to ~1 m s^{-1}) when the RI was set at 0.5 km and 2 km, and the VE was set between 50% and 90% (cf. Fig. 15). In Experiment C, significant discrepancies in 3D winds appeared by decreasing (raising) the weighting coefficient from the AWS observations (LDPAS datasets). In addition to the reasonable winds can be derived by applying the optimal setting in modified WISSDOM, 90% (50%) of VE are also recommended over complex terrain (flat surface). The results of these sensitivity testing will be helpful to verify the impacts from various scenarios in this area. The conclusions can also be good refence to decide where the best locations for the instruments employed.

This study demonstrated that reasonable patterns of 3D winds were derived by the modified WISSDOM synthesis scheme in a strong wind event. Reasonable winds can be retrieved from modified WISSDOM with sufficient coverage from the data, moderate weighting function and appropriate implements from different datasets. In the future, many cases are required to check the performance of this modified WISSDOM scheme with different synoptic weather systems under clear-air conditions in different seasons. In addition, knowing the detailed kinematic fields will help us to identify where the flow accelerates/decelerates over complex terrain. Thus, the possible mechanisms of extremely strong winds in South Korea will be well documented through combinations with derived dynamic fields (Tsai et al., 2018, 2022), thermodynamic fields (Liou et al., 2019), observations and simulations. Except for the detailed wind structures can be well documented in any meteorological phenomena under clear-air conditions (eq., land-sea breeze, micro-downburst, and non-precipitation low-pressure systems etc.). Furthermore, the new version of WISSDOM has broad applications in site surveys of wind turbines, wind energy,

771   monitoring wildfires, outdoor sports in mountain ranges and aviation security.

Code and data availability. The scanning Doppler lidars, AWS, and sounding data used in this study are available through zenodo: https://doi.org/10.5281/zenodo.6537507. The LDAPS dataset is freely available from the KMA website (https://data.kma.go.kr).

Acknowledgments. This work was supported by the National Research Foundation of Korea (NRF) grant funded by the Korea government (MSIT) (No. 2021R1A4A1032646) and by the Korea Meteorological Administration Research and Development Program under Grant KMI2022-00310.

Author contributions. This work was made possible by contribution from all authors. Conceptualization, CLT, GWL; methodology, CLT, YCL, and KK; software, CLT, YCL, and KK; validation, KK, YCL, and GWL; formal analysis, CLT, and KK; investigation, CLT, and GWL; writing—original draft preparation, CLT; writing—review and editing, GWL, YCL and KK; visualization, CLT; supervision, GWL; funding acquisition, GWL. All authors have read and agreed to the published version of the manuscript.

Competing interests. The authors declare that they have no conflict of interest.

Special issue statement. This article is part of the special issue "Winter weather research in complex terrain during ICE-POP 2018 (International Collaborative Experiments for Pyeongchang 2018 Olympic and Paralympic winter games) (ACP/AMT/GMD inter-journal SI)". It is not associated with a conference.

References

796 **References**

797 Armijo, L.: A theory for the determination of wind and precipitation velocities with Doppler

798   radars. J. Atmos. Sci., 26, 570–573. 1969.

799 Bell, M. M., Montgomery, M. T., and Emanuel, K. A.: Air–sea enthalpy and momentum

800   exchange at major hurricane wind speeds observed during CBLAST, *J. Atmos. Sci.*, **69**,

801   3197–3222, https://doi.org/10.1175/JAS-D-11-0276.1, 2012.

802 Bell, T. M., Klein, P., Wildmann, N., and Menke, R.: Analysis of flow in complex terrain using

803   multi-Doppler lidar retrievals, *Atmos. Meas. Tech.*, **13**, 1357–1371,

804   https://doi.org/10.5194/amt-13-1357-2020, 2020.

805 Chen, Y.-A.: Verification of multiple-Doppler-radar derived vertical velocity using profiler data

806   and high resolution examination over complex terrain, M.S. thesis, National Central

807   University, 91 pp., 2019.

808 Choi, D., Hwang, Y., Lee, YH.: Observing Sensitivity Experiment Based on Convective Scale

809   Model for Upper-air Observation Data on GISANG 1 (KMA Research Vessel) in Summer

810   2018. *Atmosphere*, **30**, 17–30, 2020 (Korean with English abstract).

811 Cha, T.-Y. and Bell, M. M.: Comparison of single-Doppler and multiple-Doppler wind retrievals

812   in Hurricane Matthew (2016), *Atmos. Meas. Tech.*, **14**, 3523–3539,

813   https://doi.org/10.5194/amt-14-3523-2021, 2021.

814 Choukulkar, A., Brewer, W. A., Sandberg, S. P., Weickmann, A., Bonin, T. A., Hardesty, R. M.,

815   Lundquist, J. K., Delgado, R., Iungo, G. V., Ashton, R., Debnath, M., Bianco, L., Wilczak,

816   J. M., Oncley, S., and Wolfe, D.: Evaluation of single and multiple Doppler lidar

817   techniques to measure complex flow during the XPIA field campaign, *Atmos. Meas. Tech.*,

818   **10**, 247–264, https://doi.org/10.5194/amt-10-247-2017, 2017.

819 Colle, B. A., and Mass, C. F.: High-Resolution Observations and Numerical Simulations of

820   Easterly Gap Flow through the Strait of Juan de Fuca on 9–10 December 1995. *Mon. Wea.*

821   *Rev.*, **128**, 2398–2422,

822   Cressman, G. P.: An operational objective analysis system. *Mon. Wea. Rev.*, **87**, 367–374, 1959.

823   Hill, M., R. Calhoun, H. J. S. F., Wieser, A., Dornbrack, A., Weissmann, M., Mayr, G., and

824   Newsom, R.: Coplanar Doppler lidar retrieval of rotors from T-REX, *J. Atmos. Sci.*, **67**,

825   713–729, 2010.

826   Jou, B. J.-D., Lee, W.-C., Liu, S.-P., and Kao, Y.-C.: Generalized VTD retrieval of atmospheric

827   vortex kinematic structure. Part I: Formulation and error analysis, *Mon. Weather Rev.*,

828   **136**, 995–1012, https://doi.org/10.1175/2007MWR2116.1, 2008.

829   Kim D.-J., Kang G., Kim D.-Y., Kim J.-J.: Characteristics of LDAPS-Predicted Surface Wind

830   Speed and Temperature at Automated Weather Stations with Different Surrounding Land

831   Cover   and   Topography   in   Korea. *Atmosphere*,   **11**,   1224.

832   https://doi.org/10.3390/atmos11111224, 2020.

833   Kim, J.-H., R. D. Sharman, R. D., Benjamin, S., Brown, J., Park, S.-H. and Klemp, J.:

834   Improvement of Mountain Wave Turbulence Forecast in the NOAA's Rapid Refresh

835   (RAP) Model with Hybrid Vertical Coordinate System, *Weather Forecast*, **34(6)**, 773-

836   780, https://doi.org/10.1175/WAF-D-18-0187.1, 2019

837   Lee, J., Seo, J., Baik, J., Park, S., and Han, B.: A Numerical Study of Windstorms in the Lee of

838   the   Taebaek   Mountains,   South   Korea: Characteristics   and   Generation

839   Mechanisms. *Atmosphere*, **11**, 431. https://doi.org/10.3390/atmos11040431, 2020.

840   Lee, J.- T., Ko, K.- Y., Lee, D.- I., You, C.- H., and Liou, Y.- C.: Enhancement of orographic

841   precipitation in Jeju Island during the passage of Typhoon Khanun (2012), *Atmos. Res.*,

842   **201**, 1245–1254. https://doi.org/10.1016/j.atmosres.2017.10.013, 2017.

843   Lee, W.-C., Marks, F. D., and Carbone, R. E.: Velocity track display – A technique to extract

844   real-time tropical cyclone circulations using a single airborne Doppler radar, *J. Atmos.*

845   *Ocean.   Tech.*,   **11**,   337–356,   https://doi.org/10.1175/1520-

846   0426(1994)011<0337:VTDTTE>2.0.CO;2, 1994

847   Lee, W.-C., Jou, B. J.-D., Chang, P.-L., and Deng, S.- M.: Tropical cyclone kinematic structure

derived from single-Doppler radar observations. Part I: Interpretation of Doppler velocity patterns and the GBVTD technique, *Mon. Weather Rev.*, **127**, 2419–2439, https://doi.org/10.1175/1520-0493(1999)127<2419:TCKSRF>2.0.CO;2, 1999.

Liou, Y.-C., Wang, T.-C. C., Lee, W.-C., and Chang, Y.-J.: The retrieval of asymmetric tropical cyclone structures using Doppler radar simulations and observations with the extended GBVTD technique, *Mon. Weather Rev.*, **134**, 1140–1160, https://doi.org/10.1175/MWR3107.1, 2006.

Liou, Y., and Chang, Y.: A Variational Multiple–Doppler Radar Three-Dimensional Wind Synthesis Method and Its Impacts on Thermodynamic Retrieval. *Mon. Wea. Rev.*, **137**, 3992–4010, https://doi.org/10.1175/2009MWR2980.1, 2009.

Liou, Y., Chang, S., and Sun, J.: An Application of the Immersed Boundary Method for Recovering the Three-Dimensional Wind Fields over Complex Terrain Using Multiple-Doppler Radar Data. *Mon. Wea. Rev.*, **140**, 1603–1619, https://doi.org/10.1175/MWR-D-11-00151.1, 2012.

Liou, Y., Chen Wang, T., Tsai, Y., Tang, Y., Lin, P., and Lee, Y.: Structure of precipitating systems over Taiwan's complex terrain during Typhoon Morakot (2009) as revealed by weather radar and rain gauge observations, *J. Hydrology*, **506**, 14-25. https://doi.org/10.1016/j.jhydrol.2012.09.004, 2013.

Liou, Y., Chiou, J., Chen, W., and Yu, H.: Improving the Model Convective Storm Quantitative Precipitation Nowcasting by Assimilating State Variables Retrieved from Multiple-Doppler Radar Observations. *Mon. Wea. Rev.*, **142**, 4017–4035, https://doi.org/10.1175/MWR-D-13-00315.1, 2014.

Liou, Y., Chen Wang, T., and Huang, P.: The Inland Eyewall Reintensification of Typhoon Fanapi (2010) Documented from an Observational Perspective Using Multiple-Doppler Radar and Surface Measurements. *Mon. Wea. Rev.*, **144**, 241–261, https://doi.org/10.1175/MWR-D-15-0136.1, 2016.

874   Mass, C. F., and Ovens, D.: The Northern California Wildfires of 8–9 October 2017: The Role

875   of a Major Downslope Wind Event. *Bull. Amer. Meteor. Soc.*, **100**, 235–256,

876   https://doi.org/10.1175/BAMS-D-18-0037.1, 2019.

877   Mohr, C. G., and Miller, L. J. : CEDRIC—A software package for Cartesian Space Editing,

878   Synthesis, and Display of Radar Fields under Interactive Control. Preprints, *21st Conf. on*

879   *Radar Meteorology,* Edmonton, AB, Canada, Amer. Meteor. Soc., 569–574, 1983.

880   Oue, M., Kollias, P., Shapiro, A., Tatarevic, A., and Matsui, T.: Investigation of observational

881   error sources in multi-Doppler-radar three-dimensional variational vertical air motion

882   retrievals, *Atmos. Meas. Tech.*, **12**, 1999–2018, https://doi.org/10.5194/amt-12-1999-

883   2019, 2019.

884   Park, J.-R., Kim, J.-H., Shin, Y., Kim, S.-H., Chun, H.-Y., Jang, W., Tsai, C.-L. and Lee, G.: A

885   numerical simulation of a strong windstorm event in the Taebaek Mountain Region in

886   Korea   during   the   ICE-POP   2018,   *Atmos.   Res.*,   **272**,   106158,

887   https://doi.org/10.1016/j.atmosres.2022.106158.

888   Päschke, E., Leinweber, R., and Lehmann, V.: An assessment of the performance of a 1.5 μm

889   Doppler lidar for operational vertical wind profiling based on a 1-year trial, *Atmos. Meas.*

890   *Tech.*, **8**, 2251–2266, https://doi.org/10.5194/amt-8-2251-2015, 2015.

891   Reed, T. R.: GAP WINDS OF THE STRAIT OF JUAN DE FUCA. *Mon. Wea. Rev.*, **59**, 373–

892   376, https://doi.org/10.1175/15200493(1931)59<373:GWOTSO>2.0.CO;2, 1931.

893   Ryzhkov, A., Zhang, P., Reeves, H., Kumjian, M., Tschallener, T., Trömel, S., and Simmer,

894   C.: Quasi-Vertical Profiles—A New Way to Look at Polarimetric Radar Data. *J. Atmos.*

895   *Oceanic Technol.*, **33**, 551–562, https://doi.org/10.1175/JTECH-D-15-0020.1, 2016.

896   Tsai, C., Kim, K., Liou, Y., Lee, G., and Yu, C.: Impacts of Topography on Airflow and

897   Precipitation   in   the   Pyeongchang   Area   Seen   from   Multiple-Doppler   Radar

898   Observations. *Mon. Wea. Rev.*, **146**, 3401–3424, https://doi.org/10.1175/MWR-D-17-

899   0394.1, 2018.

900 Tsai, C.-L., Kim, K., Liou, Y.-C., Kim, J.-H., Lee, Y., and Lee, G.: Orographic-induced strong

901   wind associated with a low-pressure system under clear-air condition during ICE-POP

902   2018,   *J.   Geophys.   Res.   Atmos.*,   **127**,   e2021JD036418.

903   https://doi.org/10.1029/2021JD036418, 2022.

904 Tseng, Y., and Ferziger, J.: A ghost-cell immersed boundary method for flow in complex

905   geometry. *J.   Comput.   Phys.*, **192**, 593–623, https://doi.org/10.1016/j.jcp.2003.07.024.

906   2003.

907 Yu, C., and Tsai, C.-L.: Surface Pressure Features of Landfalling Typhoon Rainbands and Their

908   Possible Causes. *J. Atmos. Sci.*, **67**, 2893–2911,

909   https://doi.org/10.1175/2010JAS3312.1, 2010.

910 Yu, C.-K., & Tsai, C.-L. : Structural and surface features of arc-shaped radar echoes along an

911   outer tropical cyclone rainband. *J. Atmos. Sci.*, **70**, 56– 72. https://doi.org/10.1175/JAS-

912   D-12-090.1, 2013.

913 Yu, C.-K., and Tsai, C.-L.: Structural changes of an outer tropical cyclone rain band encountering

914   the topography of northern Taiwan. *Q. J. R. Meteorol. Soc*, **143**, 1107–1122.

915   https://doi.org/10.1002/qj.2994, 2017.

916 Yu, C.-K., Cheng, L.-W., Wu, C.-C., and Tsai, C.-L.: Outer Tropical Cyclone Rainbands

917   Associated with Typhoon Matmo (2014). *Mon. Wea. Rev.*, **148**, 2935–2952,

918   https://doi.org/10.1175/MWR-D-20-0054.1, 2020.